WAVE LOADING ANALYSIS

OF LAKE WASHINGTON BRIDGES

VOLUME I

PREPARED FOR

WASHINGTON STATE DEPARTMENT OF TRANSPORTATION

BRIDGE & STRUCTURES ENGINEER

Under Consulting Agreement Y-2615

in collaboration with

KPFF Consulting Engineers
and Dr. Richard Reed

File No. 8306
June 1983

THE GLOSTEN ASSOCIATES, inc.
Naval Architects · Marine Engineers · Ocean Engineers

2 - 40.1

WAVE LOADING ANALYSIS

OF LAKE WASHINGTON BRIDGES

VOLUME I

PREPARED FOR

WASHINGTON STATE DEPARTMENT OF TRANSPORTATION

BRIDGE & STRUCTURES ENGINEER

Under Consulting Agreement Y-2615

in collaboration with

KPFF Consulting Engineers
and, Dr. Richard Reed

File No. 8306
June 1983

TABLE OF CONTENTS-VOLUME I

VOLUME I - Analytical Methods

1. INTRODUCTION

In January 1983 the Washington State Department of Transportation commissioned the engineering firms of The Glosten Associates, Inc. and KPFF to analyze the wave induced dynamic loads expected on each of the three Lake Washington floating bridges. The bridges to be analyzed were respectively the "third Lake Washington floating bridge" which will also be refered to within these reports as the "new I-90 bridge", and the existing Lacey V. Murrow and Evergreen Point floating bridges. The purpose of these analyses was to subject these bridges to state-of-the-art analysis to predict expected motions and internal structural loads. The Glosten Associates, Inc. were responsible for the overall technical direction of this analysis project and for the specific areas of hydrostatics, mooring lines, hydrodynamic coefficients and forces, wave hindcasting, and stochastic analysis. KPFF was responsible for the structural model including structural mass, damping and elasticity, and KPFF bore the principal responsibility for the numerical processing.

This first volume of four provides a general overview of the problem and documents the solution methods employed.

Volumes II, III and IV present the findings of this study as they respectively pertain to the new I-90 bridge, the Lacey V. Murrow bridge and the Evergreen Point bridge.

2. THEORETICAL OVERVIEW

The analysis of the dynamic responses of floating bridges, to the forces induced by realistic wind-driven wave fields, is an admittedly complex subject. With the exception of floating breakwaters there are no direct parallels elsewhere in ocean engineering. The literature on this topic is therefore not extensive. Modern literature on topics concerning the dynamic responses of marine structures is confined to that written since 1952 when the first practical analytical model for realistic irregular wave fields was developed by Dr. Willard Pierson of City University of New York, [1][1] The modern literature on the analysis of floating bridges appears to begin in 1972 with separate contributions by Professor Hartz [2] and a Ph.D. dissertation by Mukerji [3] The literature is sparse from 1972 until 1979 when the failure of the Hood Canal Bridge sparked considerable activity which has continued on to the current year.

In all there are less than a dozen individuals or teams which one would identify as contributors to the technical literature on this topic since 1972. These include Mukerji, Hartz, Tokola/Earl & Wright, Langen, Sigbjornsson, Hunziker, Georgiadis, Nachlinger & Engel, and Hutchison.

2.1 THE DOMAINS OF MODERN ANALYSIS

The structure of modern theory provides three domains of analysis for dynamic problems such as the one under consideration. These are the time domain, the frequency domain and the probability domain. These domains are related each to the other through a network of powerful theorems and transformations. Thus, for instance, a response observed in the time domain may be given a frequency domain representation through the application of a Fourier transform. Similarly one can discuss the statistics and probabilities which apply to that response, based either on information obtained in the time domain or from the frequency domain representation. Each domain of analysis provides a convenient perspective for certain types of problems·and it is likewise often advantageous to perform part of the analysis in one domain and then transform to another domain to obtain the final answers. The principal relationships between the various domains are illustrated in figure 1.

Final answers for problems such as the dynamic responses of floating bridges are usually response statistics and probabilities. Before these can be obtained it is usually

---

[1]Numbers in [ ] brackets refer to references at the end of this volume.

SHIP RESPONSE IN RANDOM SEA
Time Record: $z(t)$

RANDOM SEA
Time Record: $\mathcal{k}(t)$

TIME DOMAIN

Measurement

AUTO-CORRELATION
FUNCTION

Assumption: Linear system

$$z(t) = \int_{-\infty}^{\infty} \mathcal{k}(t-\tau)\, a_z(\tau)\, d\tau$$

where:

$$a_z(\tau) = \frac{1}{2\pi} \int_{-\infty}^{\infty} A_z(\omega)\, e^{i\omega t}\, d\omega$$

Measurement

TRANSFORMATIONS

WEINER-
KHINTCHINE
THEOREM

FOURIER
TRANSFORM

STIELTJES INTEGRALS
For ship response:

$$z(t) = \int_o^\infty A_z(\omega)\, e^{i\,[\omega t + \epsilon(\omega)]}\sqrt{s_{\mathcal{k}}(\omega)\,d\omega}$$

For random sea:

$$\mathcal{k}(t) = \int_o^\infty e^{i\,[\omega t + \epsilon(\omega)]}\sqrt{s_{\mathcal{k}}(\omega)\,d\omega}$$

(Similar)

EQUATIONS OF
MOTION IN
REGULAR WAVES

FREQUENCY RESPONSE
OPERATORS, $A_z(\omega)$

EXPERIMENTS IN
REGULAR WAVES

Assumptions:
Linear system
Superposition

FREQUENCY DOMAIN

SHIP RESPONSE SPECTRUM,

$$S_z(\omega) = \underbrace{A_z(\omega)\, *\, \overline{A_z(\omega)}}_{RAO(\omega),\ Response\ amplitude\ operator}\, *\, S_{\mathcal{k}}(\omega)$$

$S_z(\omega)$

Area $m_0 = \int_o^\infty S_z(\omega)\, d\omega$

SEA SPECTRUM

$S_{\mathcal{k}}(\omega)$

STANDARD SPECTRA

SEA OBSERVATIONS

PROBABILITY DOMAIN

Assumption: Gaussian process with zero mean

PROBABILITY FUNCTION, form based on spectral breadth
If narrow band:

$$p(z) = \frac{2\,z}{R}\, e^{-\frac{z^2}{R}} \ , \ where \ R = 8\,m_0$$

(Rayleigh distribution)

$p(z)$

Similar for $p(\mathcal{k})$

STATISTICAL PREDICTIONS OF SHIP RESPONSE

$$Pr\left\{ z > a \right\}$$

Average
Average of the 1/3 highest (Significant)
Average of the 1/10 highest
Expected maximum, etc.

Similar predictions
for wave height

$$Pr\left\{ \mathcal{k} > a \right\}$$

Analytical tools of seaway and ship motion analysis and prediction; inspired by a similar presentation by Ochi

FIGURE 1
DOMAINS OF MODERN STOCHASTIC ANALYSIS

FROM REFERENCE 13

necessary to perform analyses in either the time or frequency domains, or both.

The traditional approach in the dynamic analysis of civil structures is to begin with second order equation systems in the time domain, perform an eigen analysis and re-normalize the equation system in terms of natural modes. The resulting algebraic equation system is then solved in what amounts to a mode superposition method. Alternatively the equation system may be solved by direct stepwise integration.

These traditional methods do not apply where the homogeneous equation set contains frequency dependent coefficients. This is the situation for fluid-structure interactions at the interface of a dense fluid. The frequency dependence arises from the gravity waves generated at the fluid surface by the bridge motion response. Because of the frequency dependent coefficients the normal modes do not form an orthogonal basis in the usual sense. The time domain solutions in the presence of frequency dependent coefficients take the unattractive form of convolution integrals. The current study is a frequency domain analysis which avoids the awkward convolution integrals and permits proper treatment of the frequency dependent co-efficients.

All researchers to date have assumed two-dimensional fluid flow around transverse bridge segments. All analyses have therefore belonged to the class of two-dimensional "strip theory" methods ,whether or not they have identified themselves as such. The current study also assumes two-dimensional fluid flow and is therefore a member of the class of "strip theory" analyses.

There are numerous other detailed issues that could be dis-cussed. These include coupling between modes of response, the analytical sources and types of damping represented, and the analytical methods utilized to obtain the sectional wave forcing functions. These issues are worthy of discussion and some will be further developed later in this volume. The remaining topic which has most divided the various practi-tioners is the analytical structure of the short-crested directional wave field, and the means of proceeding from the frequency response functions to the response variance due to excitation derived from such a wave field characterized by such a directional spectrum.

The traditional school of thought, with origins in the ship dynamics theories that began evolving in the 1950's, is that the variance of the responses can be obtained through super-position of the responses to the constituent long-crested wave components which compose the directional spectrum. The other, more recently developed, school of thought maintains that the variance should be obtained from the beam sea response func-tions operating on a scalar wave spectrum and modified by a

scalar coherency function. The scalar coherency function is derived from the directional spreading function used to obtain the directional wave spectrum from the scalar wave spectrum. These two positions had the appearance of a fundamental difference. However, in a recent technical paper [4] it has been proven that the two methods are logically consistent and therefore equivalent, each one with the other. The choice of approach in this matter therefore becomes one of convenience and numerical efficiency. After examining the advantages of both approaches the method based on beam sea response functions modified by the scalar coherency function was selected for the current study based on clear advantages in computational efficiency.

2.2 Random Processes and Statistics

The responses of floating bridges to wave loads is a member of that class of problems known as random processes. In this instance, the random character has its origins in the randomness associated with the exciting wave field. The bridge response mechanism is, when viewed from a sufficiently elemental level, a purely deterministic mechanism of the type that is quite familar. The bridge "operates" on the incident random wave field, scaling the load derived from each constituent wave frequency and shifting the response phase. These responses propogate along the bridge (from the point of application of the wave impulse) as response waves. Response waves attenuate as they progress as a result of the damping processes, particularly the structural damping process. The final realization of the response process at each location is the instantaneous summation of the arriving random response signals of all frequencies from throughout the bridge.

It is instructive to regard these responses as being samples of signals obtained as part of a field instrumentation project. One can imagine instrumentation recording time domain signals of acceleration bending moment, shear, etc. Such a signal would possess the character of appearance illustrated in figure 2. The mean signal value depicted in figure 2 would represent the static response due to steady loads such as wind and current. The wave induced dynamic response oscillates about the mean signal. It is this oscillatory portion of the signal which we wish to subject to closer examination. Accordingly, following the principle of superposition, the mean (steady) signal is subtracted from the original signal to obtain a zero-mean process signal such as shown in figure 3.

The point of view adopted for describing this random zero-mean process signal is statistical. We shall seek statistical descriptions of the signal, particularly those which provide insight into the extreme values which the signal may attain.
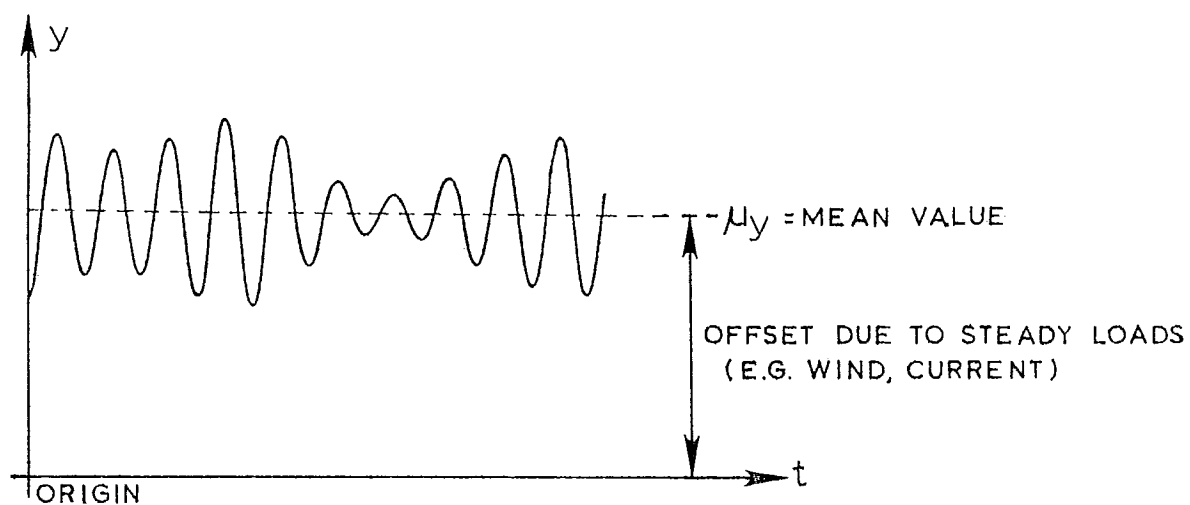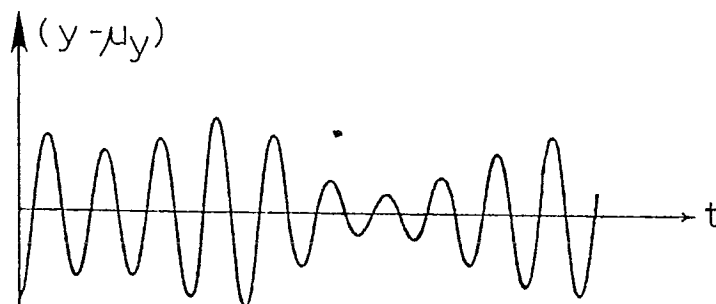
5

FIGURE 2

RANDOM SIGNAL WITH NON-ZERO MEAN

FIGURE 3

RANDOM SIGNAL WITH MEAN REMOVED

The first pertinent observation in pursuit of this objective is that the signal itself is distributed according to the familiar Gaussian (normal) probability distribution with zero-mean and variance, σ^2_{yy}

$$\sigma^2_{yy} = \frac{1}{2T} \int_{-T}^{T} [y(t)]^2 dt$$

This variance is identical to the zero-order moment of the response variance spectrum

$$\sigma^2_{yy} = m^{(o)}_{yy} = \int_{0}^{\infty} S_{yy}(\omega) \ d\omega$$

This identity is one of the principal foundations of the frequency domain analysis of random processes.

Having obtained a convenient expression for the variance of our zero mean Gaussian process, the probability density for the instantaneous process ordinates in continuous time is known:

$$p(y) = \frac{1}{\sqrt{2\pi\sigma^2_{yy}}} e^{\{-y^2/2\sigma^2_{yy}\}}$$

The local maxima of the process occur wherever $\frac{dy}{dt} = 0$ as shown in figure 4. As indicated in figure 4, the extreme positive and negative values of the process occur once each per process cycle (as measured by the process zero-crossings). The probability distribution for the maxima has a generalized Rayleigh distribution (figure 5), which depends on the spectral bandwidth parameter, ϵ. If the spectral bandwidth is small (i.e. $\epsilon \approx 0$) then the probability density function for the maxima approaches the Rayleigh distribution:

$$p(\xi) = \xi \ e^{-\frac{\xi^2}{2}} \ , \ 0 < \xi < \infty$$

where: $\xi = $ (local maxima of y)$/ \sqrt{\sigma^2_{yy}}$

and if the spectral bandwidth is large (i.e. $\epsilon \to 1$) then the probability density function for the maxima approaches the normal distribution.
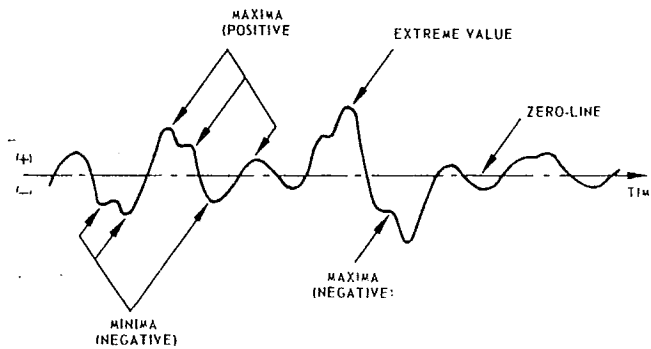
7

HE GLOSTEN ASSOCIATES, inc.

Fig. 1 Explanatory sketch of a random process $X(t)$

FIGURE 4
SKETCH SHOWING LOCAL PROCESS
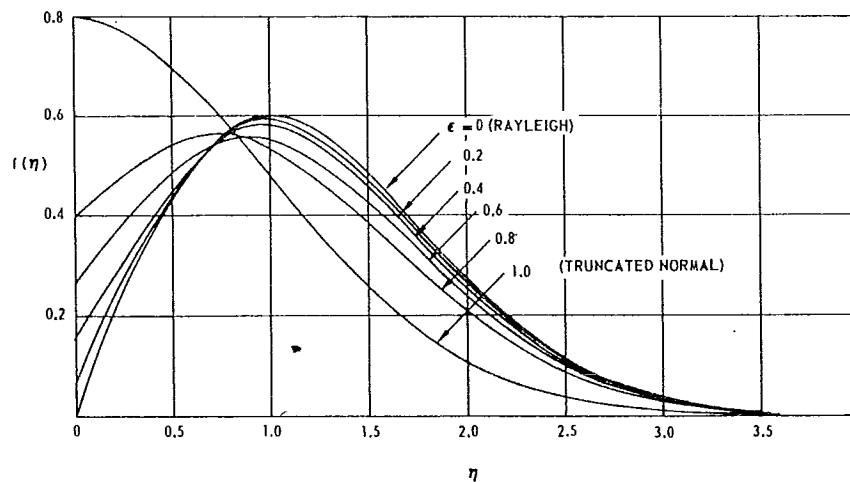## MAXIMA AND EXTREME VALUES
FROM OCHI (REFERENCE 5)

Fig. 2 Probability density function of random variable H as a function of bandwidth parameter ϵ

FIGURE 5
GENERALIZED RAYLEIGH DISTRIBUTION
FROM OCHI (REFERENCE 5)

Common statistics which describe these processes are the average of
the highest 1/3rd responses ("significant" response) and the
average of the highest 1/10th responses. These are the centroids
of the portions of the probability density distributions associated
with respectively one-third and one-tenth of the area under the
probability density curve as illustrated in figure 6.

Extreme values are obtained using order statistics which consider
the probability distributions appropriate to these subsets of the
maxima which are the largest in N process cycles (e.g. N = 1000
cycles) or in a specified period of observation, T (e.g. T = 1
hour). These extreme values have a distribution such as
illustrated in figure 7. The most probable extreme value
corresponds to the peak (mode) of the extreme value distribution.
As can be seen by the large area to the right of the peak under the
extreme value distribution, there is a large probability of
exceeding the most probable extreme (typically about a 0.632
probability of exceedance). For this reason it is good practice to
work to a confidence level (e.g. 90% confidence) where the
probability of exceeding the expected extreme value is suitably
small (e.g. probability of exceedance α = 0.10). This is also
depicted in figure 7.

The statistics described above can be estimated from the variance
of the response process using so-called "Rayleigh factors". These
are ratios of the response values at the various statistical levels
to the root of the response variance.

TABLE 2-1

Narrow Band Process, $\epsilon \approx 0$, Response Ratios

Statistical Level	Rayleigh Factor = $Y/\sqrt{\sigma_{yy}^2}$
Most Frequent (Mode)	1.00
Average (Mean)	1.25
Significant (Avg. 1/3 highest)	2.00
Averag of Highest 1/10	2.55
Most Probable Extreme (1000 cycles)	3.72
90% Confidence Extreme (1000 cycles)	4.29

Refinements of these ratios to reflect actual spectral bandwidth
exist. The reader interested in these issues should consult Ochi
[5].

For the current bridge response studies the extremes were formu-
lated in terms of the expected extremes in one-hour of
exposure. The actual factors used to estimate the extremes
therefore vary slightly from process to process depending on the
average zero-crossing period of the process. A process with
precisely 1000 cycles in one hour would possess an average zero-
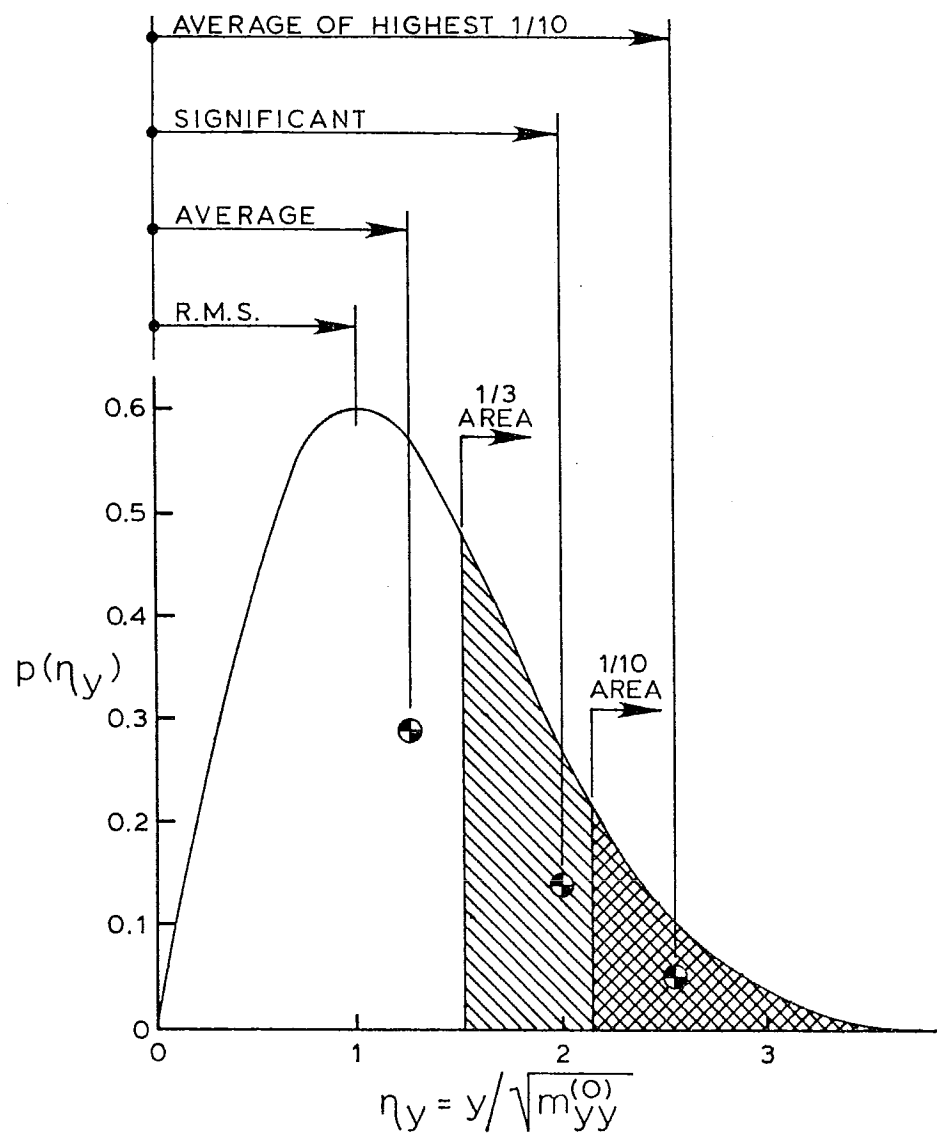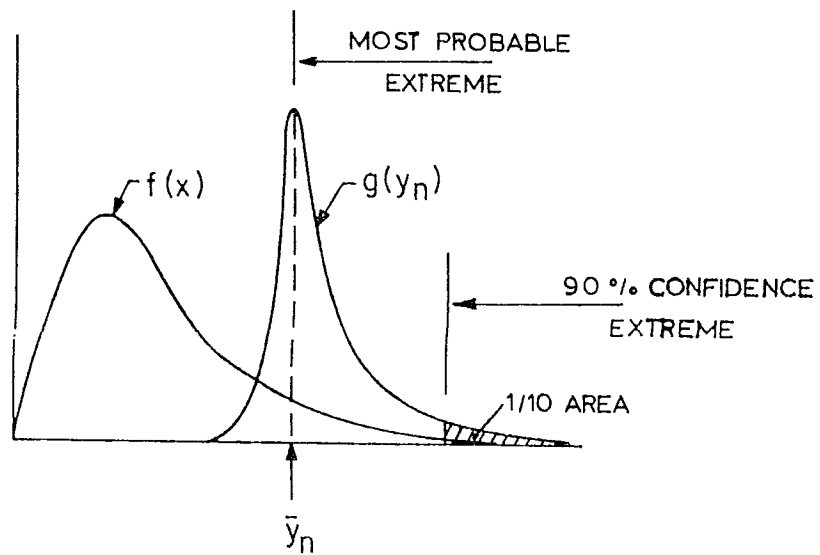crossing period of 3.6 seconds.

FIGURE 6

RAYLEIGH PROBABILITY DISTRIBUTION SHOWING
STATISTICS OF MAXIMA OF RANDOM FUNCTION
RELATED TO CENTROIDS OF AREAS

Explanatory sketch of initial
probability density function f(x) and
extreme value probability function g(y_n)

FIGURE 7
EXTREME VALUE PROBABILITY DISTRIBUTIONS

2.3 Dynamic Analysis of Wave Loading

In order to analyze the dynamic response of a long elastic structure such as a floating bridge a finite element structural model is developed representing the salient features of the structural geometry in terms of nodes and structural elements connecting those nodes. The structural models developed for this study assign the physical properties of mass, damping and restoring force to the nodes. The structural elasticity is the result of uniform structural properties extending over each structural element but the final stiffness matrix as it enters into the equations of motion represents the resolution of these elastic structural properties to the nodes. The vector of wave forcing functions is developed for each node to compose the right-hand side of the equation system. Each of the topics which enter into the formulation of the equation system is further developed in subsequent sections of this volume.

$$[M+A(\omega)]\,\ddot{\vec{x}} + [B_1(\omega)]\,\dot{\vec{x}} + [B_2]\frac{\ddot{\vec{x}}}{\left|\dot{\vec{x}}\right|}\left|\dot{\vec{x}}\right| + [K+C]\,\vec{x} = \vec{f}(\omega)\,e^{i\omega t} \quad (1)$$

where: M is the structural mass-inertia matrix

$A(\omega)$ is the frequency dependent "added mass" matrix

$B_1(\omega)$ is the hydrodynamic damping matrix

B_2 is the hysteretic structural damping matrix, in-phase with the velocity and proportional to relative displacements.

K is the structural stiffness matrix representing the elastic properties including the effects of mooring lines

C is the hydrostatic stiffness matrix representing the hydrostatic restoring forces

$\vec{f}(\omega)$ is the frequency dependent complex amplitude vector for wave forces and moments

$\vec{x}$ is the complex-valued vector of nodal displacements

$\dot{\vec{x}}$ and $\ddot{\vec{x}}$ are time derivatives of $\vec{x}$ for velocity and acceleration respectively

and ω is the circular frequency in radians per second

such that $\omega = 2\pi f = 2\pi/T$

where: f is the frequency in cps

T is the period in seconds

The governing equation system is therefore a system of second order ordinary differential equations for the motion displacements of each node of the finite element structural model. At each discrete frequency for which the equation system is developed the coefficients are constant, though of course the hydrodynamic coefficients vary from one discrete frequency to the next. Internal structural loads of shear and bending moment are obtained from the relative motion between adjacent nodes and the structural stiffness matrix, once the equation system has been solved for the nodal displacements.

At each frequency for which the analysis is to be performed the equation system is solved in the complex phase plane by the method of undetermined coefficients. The solution is accomplished by first substituting a complex amplitude harmonic vector and factoring the coefficient matrix on the left-hand side of the equation system. Once the inverse of this coefficient matrix is obtained, the undetermined complex amplitude vector can be obtained for any particular loading. This is done for load vectors acting in isolation at each node in successive turn to obtain a set of response vectors, one vector for each node in the structural model subject to wave loading. This analysis is repeated for each discrete frequency of wave excitation under consideration. The resulting set of response solution vectors are denoted as shown below and may be referred to as the "impulse response functions". (See ref. 4)

$$X_\alpha(\omega, \theta, j; k)$$

where: α is the mode of response e.g. sway translation, roll rotation, or vertical bending moment

          θ is the wave heading angle ($90° = \frac{\pi}{2}$ radians is beam seas)

          j is the node index number where the response occurs

          k is the node index number where the wave force impulse is applied

These "impulse response functions" form the fundamental solution set for subsequent stochastic analysis. The impulse response functions are the dynamic analogs of the more familiar static counterparts, the influence coefficients. In fact, the impulse response functions for $\omega = 0$ are the static influence coefficients. The impulse response function represents an extension to many degrees of freedom, of the frequency response functions (also sometimes refered to as the "response amplitude operators"), that are familiar in more traditional ship dynamics. The reader wishing greater detail on the solution methods should refer to the section of this volume on "Numerical Processing" and may also find reference 4 to be of assistance.

Once the impulse response functions have been been obtained the stochastic analysis can be performed. The objective of this phase of the analysis is to obtain the first three even moments of the response spectrum (or response cross spectrum) for each response of interest. From these moments the response statistics and probabilities can be determined.

As a first step towards obtaining the response spectral moments the response spectral densities are defined as follows:

$$S_{\alpha\beta}(\omega,j;\ell) = X_{\alpha}(\omega,\tfrac{\pi}{2},j;k)\ \overline{X_{\beta}(\omega,\tfrac{\pi}{2},j;\ell)}\ S_{\zeta\zeta}(\omega)\ \sqrt{\gamma_{k\ell}(\omega)}$$

(2)

where : $\gamma_{k\ell}(\omega)$ is the complex scalar coherency function

       $S_{\zeta\zeta}(\omega)$ is the scalar wave spectral density function

The spectral moments are obtained as the summation of complex-valued integrals over the range of possible combinations of jointly excited nodes:

$$m_{\alpha\beta}^{n}(j) = \sum_{k}\sum_{\ell}\left\{\int_{0}^{\infty}X_{\alpha}(\omega,\tfrac{\pi}{2},j;k)\ \overline{X_{\beta}(\omega,\tfrac{\pi}{2},j;\ell)}\ \omega^{n}S_{\zeta\zeta}(\omega)\ \sqrt{\gamma_{k\ell}(\omega)}\,d\omega\right\}$$

(3)

where : $m_{\alpha\beta}^{n}(j)$ is the nth cross spectral moment between response modes α and β as seen at node j

3. COORDINATES AND CONVENTIONS

The coordinate systems used are right-handed orthogonal coordinate systems with the x-axis directed along the major longitudinal axis of the subject floating bridge. The x-y plane is coincident with the static waterplane and the z-axis is directed in the vertical direction with the positive sense corresponding to up.

The analysis is performed in a F-L-T system of units with the basic unit of force being kips, the basic unit of length being feet, and the basic unit of time being seconds. Frequencies quoted throughout the study are circular frequencies, ω, in radians per second. Specific details of the coordinate systems and origins are defined in subsequent volumes for each bridge.

4. STRUCTURAL MODELING

The stiffness, mass and damping matrices used in the equations of motion were developed using the "direct stiffness method". Each bridge is discretized into several hundred elements joining together at nodes. Each node has six degrees of freedom, three translational and three rotational. These finite elements are assigned stiffness and damping properties which correspond to the section of the bridge which they represent. An extensive discussion of the techniques used for modeling the structural damping is given in Section 5.

The masses are idealized as lumped at the nodes. The hydrostatic stiffness and hydrodynamic mass, damping and forcing functions were also applied at the nodes. The nodes are located vertically at the structural center of the bridge. Properties developed at other locations, i.e. the nominal waterplane (x-y axis plane) were subjected to a transformation to the nodal location.

4.1 Moorings

Mooring lines were analyzed as elastic-catenaries using programs developed specifically for this task which were executed on the HP-83 computer. A recursive solution strategy is employed. The algorithms utilized solve the catenary equations and update the length of the mooring cable to account for elastic extension due to load. The weight per foot of the cable is updated to reflect conservation of cable mass on the extended length, and the catenary equations are solved again. The procedure terminates when a set of non-dimensionalized error terms have been reduced below 0.0005.

The mooring line analysis proceeds in three stages for each line. The first stage solves for the "free" (i.e. unloaded) cable length that satisfies the geometry and design static tension conditions at the design lake level. In the second stage the free cable length is held constant and the lake level is dropped to 3 feet below design lake level. The catenary problem is again solved. In the third and final stage of analysis the pontoon is shifted horizontally a specified increment intended to represent the mean "static" horizontal offset due to a steady wind corresponding to the greatest 100 year wind speed determined in the climatological analysis. This shift tends to tighten the upwind mooring cables and slacken the downwind cables. The catenary problem is again solved at this new shifted position and the cable tension and direction vectors at the point of attachment to the pontoon are determined.

Cable axial stiffness about the solution point obtained in the third stage of analysis is determined in the following manner. A new coordinate system is established with the u-axis directed along the direction vector at the pontoon attachment point obtained in the third stage of analysis and with the origin located at that solution point. An array of twenty-one points is

16

established along the u-axis consisting of ten positive u-displacements (tightening), ten negative u-displacements (slackening) and the origin. The catenary problem is solved at each of these points and the axial stiffness acting at the origin is determined using a five-point Lagrange numerical differentiation procedure.

A sample computer output for the entire three step analysis procedure on a typical cable from the new I-90 bridge is shown in figure 8. Figure 9 shows a plot of the axial tension vs. displacement in the u-direction as obtained in the example cable analysis.

17

CATENARY SOLUTION   PAGE 1 OF 2

ANCHOR LINE L-S
COORDINATES AT PONTOON (FEET)
```
    X              Y              Z
  3752.75       -32.95          0.00
```

COORDINATES AT ANCHOR (FEET)
```
    X              Y              Z
  3752.75      -537.50        -189.02
```

CABLE AREA = 3.38 SQ.IN.   MODULUS OF ELASTICITY = 23.00E+006 PSI
UNLOADED WT/FT OF LINE = 9.86 LBS/FT
HORIZONAL PRETENSION = 120.00E+003 LBS

LAKE LEVEL = 8.02 FT
============================
HORIZONAL PRETENSION 120.00E+003 LBS
VERTICAL TENSION = 476.14E+002 LBS
TENSION ALONG LINE = 129.10E+003 LBS

FREE LENGTH = 537.93 FT   LOADED LENGTH = 538.83 FT
K0= 504.55   B0= 189.02
WT/FT OF LINE = 9.84
ANGLE FROM HORIZONAL = 21.64 DEG   DROOP ANGLE = 1.10 DEG
DIRECTION COSINES
X-DIR = 0.0000   Y-DIR = -.9295   Z-DIR = -.3688

LAKE LEVEL DROPPED   3.00 FEET
==
TARGET WATER DEPTH = 186.02 FT   CALCULATED WATER DEPTH = 186.02 FT
LENGTH OF LINE = 538.19 FT
WT/FT OF LINE = 9.86 LBS/FT
HORIZONAL PRETENSION = 333.84E+002 LBS   TENSION ALONG LINE = 365.92E+002 LBS
ANGLE FROM HORIZONAL = 24.17 DEG   DROOP ANGLE = 3.93 DEG
DIRECTION COSINES
X-DIR = 0.0000   Y-DIR = -.9123   Z-DIR = -.4095

 BRIDGE DISPLACED .46 FEET (3.00 FEET BELOW DESIGN LAKE LEVEL)
===

K0= 504.55 FT   K4= 505.01 FT   K= 505.01 FT
LENGTH OF LINE = 538.34 FEET
WT/FT OF LINE = 9.85
HORIZONAL PRETENSION = 545.75E+002 LBS   TENSION ALONG LINE = 591.34E+002 LBS
ANGLE FROM HORIZONAL = 22.65   DROOP ANGLE = 2.42
DIRECTION COSINES
X-DIR = 0.0000   Y-DIR = -.9229   Z-DIR = -.3850

FIGURE 8
Typical Mooring Cable Analysis
New I-90 Bribge, cable L-S

THE GLOSTEN ASSOCIATES, inc.   18

NEW I-90 BRIDGE

CATENARY SOLUTION   PAGE 2 OF 2

ANCHOR LINE L-S

DETERMINE STIFFNESS   3.00 FEET BELOW DESIGN LAKE LEVEL   (AT .46 FEET HORIZ. DISPLACEMENT)
==

DIRECTION COSINES
X-DIR = 0.0000   Y-DIR = -.9229   Z-DIR = -.3850
ANGLE FROM HORIZONAL = 22.65 DEG   DROOP ANGLE =   2.42 DEG

U(FEET)	TENSION (LBS)	H. TENSION
-2.500	16376	14305
-2.250	17224	15111
-2.000	18232	16069
-1.750	19453	17226
-1.500	20964	18656
-1.250	22895	20482
-1.000	25465	22908
-.750	29089	26325
-.500	34606	31520
-.250	43683	40057
0.000	59380	54806
.250	83634	77581
.500	114285	106352
.750	147778	137785
1.000	182585	170449
1.250	218011	203691
1.500	253700	237180
1.750	289373	270652
2.000	325406	304461
2.250	361227	338072
2.500	397256	371876

AXIAL STIFFNESS AT U= 0.0
=========================
   79651 LBS/FT

FIGURE 8, Continued

PONTOON

+u

W.L. ▽

ANGLE FROM
HORIZONTAL

ORIGIN OF
u-AXIS

DEFINITIONS

TENSION, KIPS

400

300

ASYMPTOTE (AE/L)

200

AXIAL STIFFNESS AT u=0
(DETERMINED BY 5-POINT
LAGRANGE NUMERICAL
DERIVATIVE)

100

$\Delta u \dfrac{dT}{du}$

Δu

U, FEET
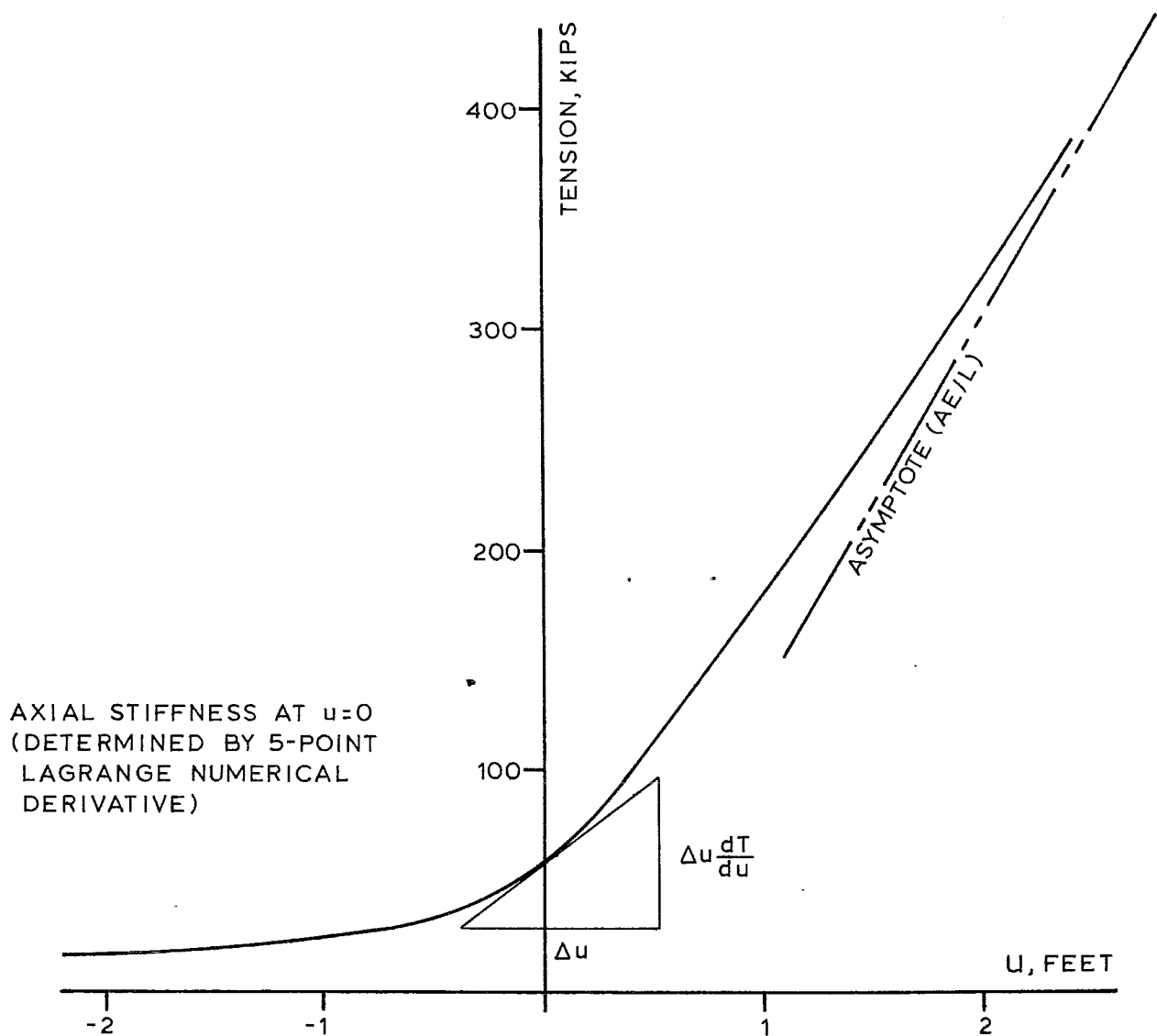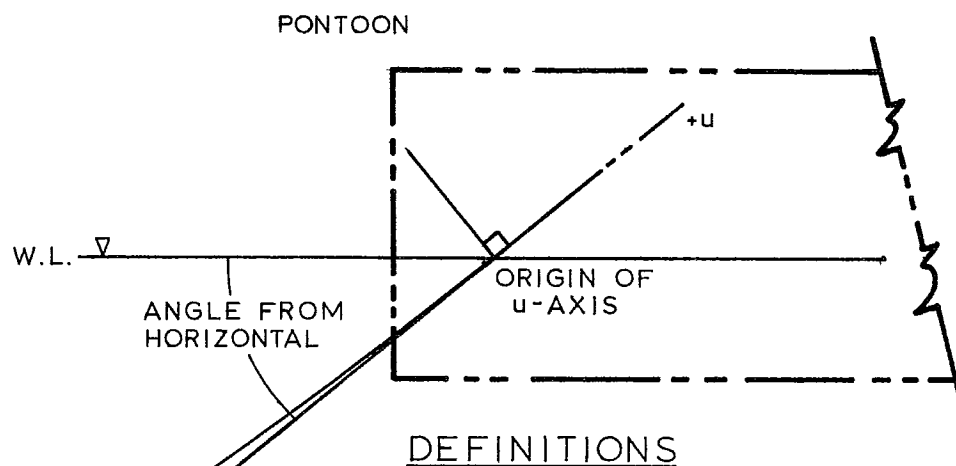
-2   -1   1   2

FIGURE 9
TYPICAL MOORING CABLE CHARACTERISTICS
(FOR ANCHOR L-S, NEW I-90 BRIDGE)

5.   STRUCTURAL DAMPING[2]

The basic energy dissipation mechanisms for structures are seldom
fully understood and are usually evaluated by experimental
measurements. The common form of representing structural damping
is viscous damping. This is a velocity dependent form, as is the
hydrodynamic damping presented elsewhere in this report. Most
literature reports damping as a ratio of critical damping.
Critical damping for a single degree of freedom system can be
expressed as:

$$C_{critical} = 2\sqrt{km}$$

Equations of motion for this project were developed on an
elemental stiffness basis but a nodal (lumped) mass formu-
lation. This formulation is quite accurate for the small nodal
spacing used. However, it introduces some difficulty in
formulating viscous damping. In a problem such as this, the
structure not only experiences relative velocities due to
structure vibrations, but it also undergoes rigid body motions
similar to a ship on an ocean. For this reason we chose to use
displacement dependent (mass independent) hysteretic damping.
The mathematical model for hysteretic damping is presented in
Section 5.3. Calibration of the structure for equivalent viscous
damping ratio, represented by the hysteretic model, is discussed
in 5.4.

5.1   The Impact of Structural Damping on Response

Structural damping was initially thought to be relatively
unimportant due to the seemingly large values of hydrodynamic
viscous damping available. Because of this the first run for the
new I-90 bridge was run without structural damping. The results
were large responses and the plots of spectral density vs.
frequency were quite spiked.

The bridge was subsequently run at $.06\pi$ and $.02\pi$ hysteretic
damping (roughly equal to 10.2% and 3.4% of critical viscous
damping). The results are as follows for node 89:

Hysteretic Damping	Vertical Bending Moment
0	103,000 k-ft
$.02\pi$	62,000
$.06\pi$	41,000

The structural damping causes substantial reduction in the

---

[2] Substantial portions of this section on structural damping are
taken directly from DYNAMICS OF STRUCTURES by Clough and Penzien
[15].

response. The amount of reduction seems to be approximately the same for all modes of response and locations along the bridge.

Figure 15 shows spectral density vs frequency for the undamped and $.02\pi$ and $.06\pi$ damped cases at node 89. The peaks are impacted more than the valleys, also the higher frequencies more than the lower ones. These results are consistent with damping theory.

5.2 Choice of Damping Ratios

SR-90 bridge results indicates that the value of structural damping is a relatively sensitive variable. The choice of damping coefficient thus becomes important. Table 3 of Earthquake Spectra and Design by Newmark and Hall, EERI, gives recommended viscous damping ratios:

RECOMMENDED DAMPING VALUES

Stress Level	Type and Condition of Structure	Percentage Critical Damping
Working stress, no more than about 1/2 yield point	Vital piping: Welded steel, pre stress concrete, well reinforced concrete (only slight cracking):	1 to 2
		2 to 3
	Reinforced concrete considerable cracking:	3 to 5 ←
	Bolted and/or riveted steel, wood structures with nailed or bolted joints:	5 to 7
At or just below yield point	Vital piping: Welded steel, pre-stressed concrete (without complete loss to prestress):	2 to 3
		5 to 7
	Prestressed concrete with no prestress left:	7 to 10
	Reinforced concrete:	7 to 10 ←
	Bolted and/or riveted steel, wood structures with bolted joints:	10 to 15
	Wood structures with nailed joints:	15 to 20

They recommended 3 to 5% of critical damping for reinforced concrete at 1/2 yield and 7 to 10% near yield. Thus the problem becomes distinctly nonlinear. Based on the values published in table 3, we would recommend the use of $.02\pi$ hysteretic damping (approximately 3.4% viscous) for responses below the survival storm. In the extreme value, 10% probability in 1 hour of a 100

year storm, we would recommend that .06 hysteretic damping (approximately 10.2 viscous) as the structure is probably at or near its yield capacity.

5.3 Hysteretic Damping

Although in many cases the viscous-damping mechanism leads to a convenient form of the structural equation of motion, the results of experiments seldom correspond closely with this type of energy-loss behavior. In some cases, the equivalent viscous-damper concept defined in terms of energy loss per cycle provides a reasonable approximation of experimental results. But, the essential frequency dependence of the viscous mechanism is at variance with a great deal of test evidence, much of which indicates that the damping forces are nearly independent of the test frequency.

A mathematical model which has this property of frequency independence is provided by the concept of hysteretic damping, which may be defined as a damping force in phase with the velocity but proportional to the displacements. This force-displacement relationship may be expressed as:

$$f_D = \xi k \, |v| \frac{\dot{v}}{|\dot{v}|} \tag{4}$$

where ζ is the hysteretic damping coefficient which defines the damping forces as a fraction of the elastic-stiffness forces. The force-displacement diagram for hysteretic damping during a cycle of harmonic displacement is depicted in Fig. 10. It will be noted that the damping resistance is similar to the linear elastic forces during displacements of increasing magnitudes but that the sense of the damping force reverses when the displacements diminish. The hysteretic energy loss per cycle given by this mechanism is:

$$w_D = 2\xi k \rho^2 \tag{5}$$

If this hysteretic energy loss is assumed to be represented by an equivalent viscous damper, the equivalent viscous-damping ratio is given by:

$$\xi = \frac{c}{c_c} = \frac{w_D}{4\pi w_s} \tag{6}$$

where w_s is the strain energy, or area under the static force-displacement diagram:
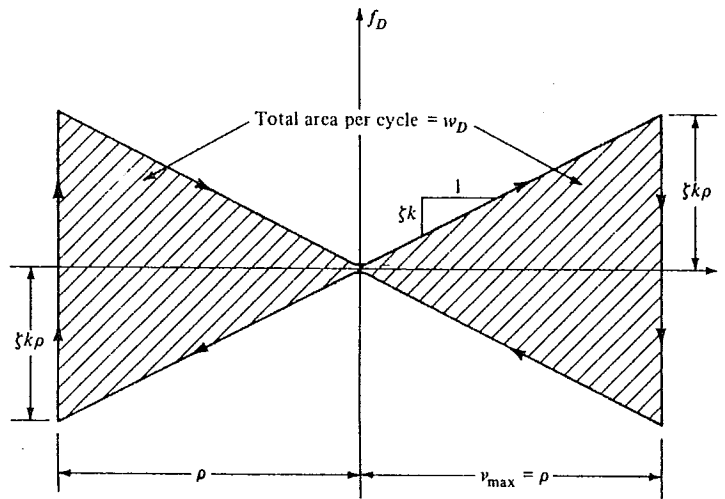
$$k = \frac{2w_s}{\rho^2} \tag{7}$$

FIGURE 4-17
Hysteretic damping force vs. displacement.

FIGURE 10
HYSTERETIC DAMPING FORCE VS DISPLACEMENT

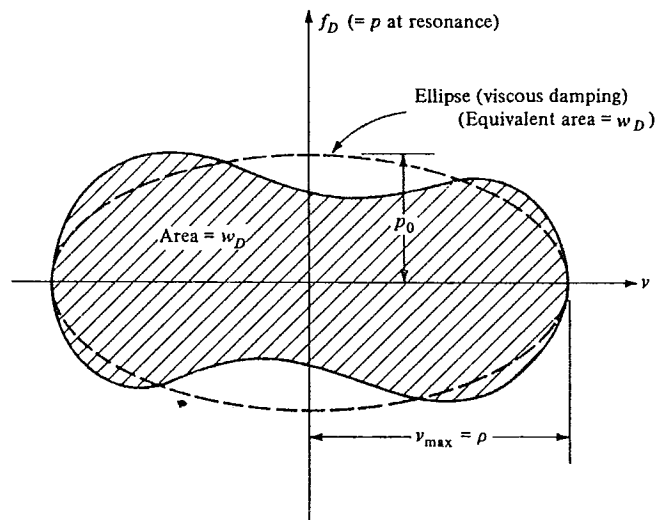FROM "DYNAMICS OF STRUCTURES" BY CLOUGH AND PENZIEN (REFERENCE 15)

FIGURE 4-15
Actual and equivalent damping energy per cycle.

FIGURE 11
ACTUAL AND EQUIVALENT DAMPING ENERGY PER CYCLE

FROM "DYNAMICS OF STRUCTURES" BY CLOUGH AND PENZIEN (REFERENCE 15)

24

In other words, Eq. (6) can be used to express the damping ratio of a structure regardless of the actual internal-energy loss mechanism. However, if the specific hysteretic-damping coefficient corresponding to a given test is to be determined, this may be expressed in terms of the damping ratio ,by substituting Eq. (5) and (7) into Eq. (6), as:

$$\zeta = \pi\xi \qquad (8)$$

Hysteretic damping results in a convenient and consistent formulation of damping even while undergoing rigid body motions. The question arises, how does this relate to viscous damping? The equation from Clough is derived by equating the work lost per cycle. See Figs. 10 and 11. From this he concludes that the hysteretic damping ratio is equal to π times the viscous damping ratio. It is apparent that the two different formulations have a different shape. This, it will be shown, results in different near-resonant displacement response for equal work dissipation.

5.4   Damping Calibration with the Eleven Node Model

The hysteretic formulation was tested, and the damping ratio used was calibrated against the classic single degree of freedom viscous damping theory. The single pontoon eleven node model was used. The ends were pinned against translation, and no anchor cables, hydrostatic or hydrodynamic terms of any kind were used. In other words, the pontoon was represented as a simple beam with mass. A forcing function in the z direction was applied at varying frequencies. Hysteretic damping ratios were varied from zero to 0.3π.

The results were compared with three measures of viscous damping in the frequency domain for a single degree of freedom system: resonant amplification, half-power (Band-width), and phase angle response.

5.4.1   Resonant Amplification

The other principal techniques for evaluating damping are based on observations of steady-state harmonic response behavior and thus require a means of applying harmonic excitations to the structure at prescribed frequencies and amplitudes. With such equipment the frequency-response curve for the structure can be constructed by applying a harmonic load $p_o \sin(\omega t)$ at a closely spaced sequence of frequencies which span the resonance frequency and plotting the resulting displacement amplitudes as a function of the applied frequencies. A typical frequency-response curve for a moderately damped structure is shown in Fig. 12.

The dynamic magnification factor for any given frequency is the ratio of the response amplitude at that frequency to the zero-
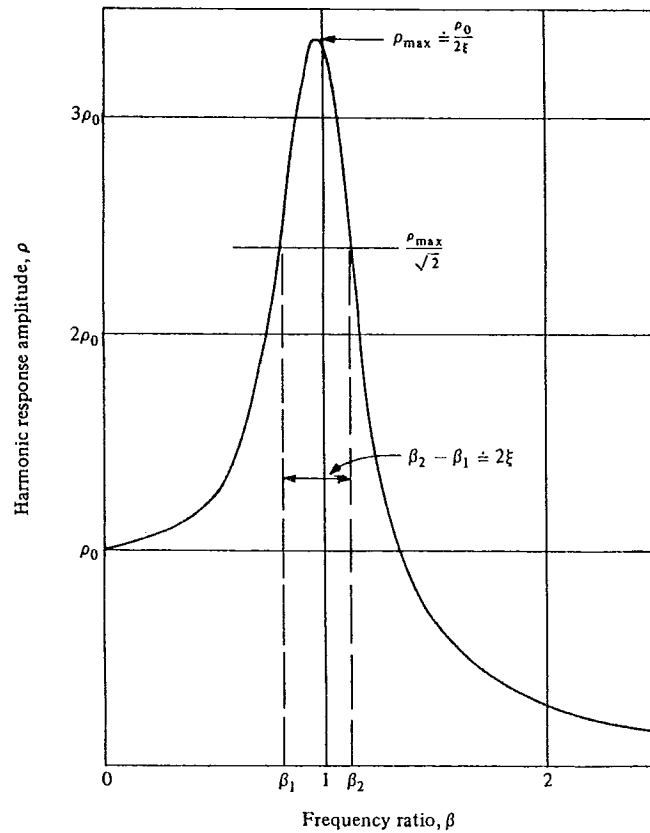
Harmonic response amplitude, ρ

$\rho_{max} \doteq \dfrac{\rho_0}{2\xi}$

$3\rho_0$

$\dfrac{\rho_{max}}{\sqrt{2}}$

$2\rho_0$

$\beta_2 - \beta_1 \doteq 2\xi$

ρ_0

0 β_1 1 β_2 2

Frequency ratio, β

FIGURE 4-14
Frequency-response curve for moderately damped system.

FIGURE 12
HALF POWER BAND-WIDTH METHOD FREQUENCY-RESPONSE CURVE FOR MODERATELY DAMPED SYSTEM

FROM "DYNAMICS OF STRUCTURES" BY CLOUGH AND PENZIEN (REFERENCE 15)

factor at resonance. When the static-response and the resonant-response amplitude are denoted by ρ_0 and $\rho_{\beta=1}$, respectivly, the damping ratio is given by:

$$\zeta = \frac{1}{2} \frac{\rho_0}{\rho_{\beta=1}}$$

(9)

5.4.2 Half-Power (Bandwidth) Method

It is evident from the general harmonic-response expression (Eq. 17) that the shape of the entire frequency-response wave is controlled by the amount of damping in the system; therefore, it is possible to derive the damping ratio from many different properties of the curve. One of the most convenient of these is the bandwidth, or half-power, method, in which the damping ratio is determined from the frequencies at which the response is reduced to $(1/\sqrt{2})\rho_{\beta=1}$;that is, at the frequencies for which the power input is half the input at resonance.

The values of these half-power frequencies can be determined by setting the response amplitude in Eq. (17) equal to $1/\sqrt{2}$ times the resonant amplitude. That is:

$$\frac{1}{\sqrt{2}} \frac{\rho_0}{2\xi} = \rho_0 [\frac{1}{(1 - \beta^2)^2 + (2\xi\beta)^2}]^{1/2}$$

(10)

or, squaring both sides:

$$\frac{1}{8\xi^2} = \frac{1}{(1 - \beta^2)^2 + (2\xi\beta)^2}$$

(11)

Solving for the frequency ratio then gives:

$$\beta^2 = 1 - 2\xi^2 \pm 2\xi\sqrt{1 + \xi^2}$$

(12)

from which (neglecting ξ^2 in the square-root term) the two half power frequencies are:

$$\beta_1{}^2 = 1-2\xi-2\xi^2 \qquad \beta_1 = 1-\xi-\xi^2$$
$$\beta_2{}^2 = 1+2\xi-2\xi^2 \qquad \beta_2 = 1+\xi-\xi^2$$

(13)

Hence, the damping ratio is given by half the difference between these half-power frequencies:

$$\xi = \frac{1}{2} (\beta_2-\beta_1)$$

(14)

This method of evaluating the damping ratio also is illustrated with the typical frequency-response curve of figure 12. A horizontal line has been drawn across the curve at 1/2 times the resonant-response value; the difference between the frequencies
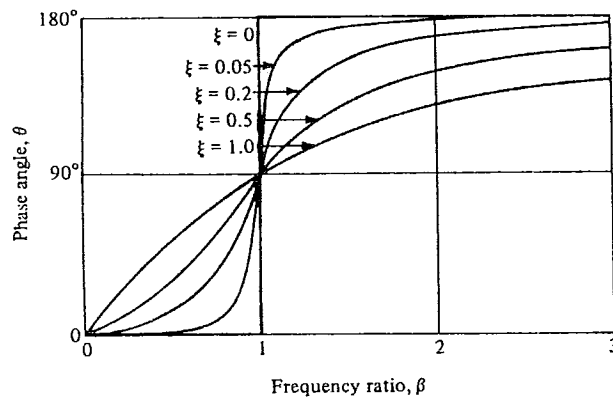
FIGURE 4-5
Variation of phase angle with damping and frequency.

FIGURE 13

VARIATION OF PHASE ANGLE WITH DAMPING AND FREQUENCY

FROM "DYNAMICS OF STRUCTURES" BY CLOUGH AND PENZIEN (REFERENCE 15)
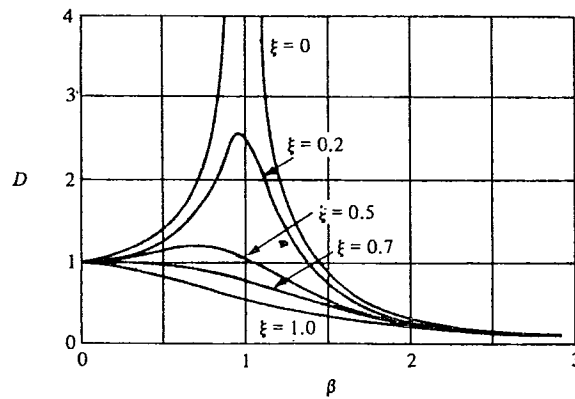

FIGURE 4-4
Variation of dynamic magnification
factor with damping and frequency.

FIGURE 14

VARIATION OF DYNAMIC MAGNIFICATION FACTOR WITH DAMPING AND FREQUENCY

FROM "DYNAMICS OF STRUCTURES" BY CLOUGH AND PENZIEN (REFERENCE 15)

at which this line intersects the response curve is equal to
twice the damping ratio. It is evident that this technique
avoids the need for the static response; however, it does require
that the response curve be plotted accurately in the half-power
range and at resonance.

5.4.3 Phase Angle Response

The phase angle θ by which the response lags behind the applied
load, as shown in figure 13, is given by:

$$\theta = \tan^{-1} \frac{2\xi\beta}{1 - \beta^2} \tag{15}$$

β represents the ratio of the applied load frequency to the
natural free-vibration frequency; i.e.:

$$\beta \equiv \frac{\bar{\omega}}{\omega} \tag{16}$$

ρ is the amplitude of the steady-state response:

$$\rho = \frac{p_0}{k} [(1 - \beta^2)^2 + (2\xi\beta)^2]^{-1/2} \tag{17}$$

Note: $\dfrac{p_0}{k}$ = static ($\omega = 0$) deflection

The ratio of the resultant response amplitude to the static
displacement which would be produced by the force p_0 will be
called the dynamic magnification factor D, figure 14; thus:

$$D = \frac{\rho}{p_0/k} = [(1 - \beta^2)^2 + (2\beta\xi)^2]^{-1/2} \tag{18}$$

The results for $.02\pi$ hysteretic damping by the three different
methods are:

Method	Equivalent viscous damping as ratio to critical:
Peak Magnification, D = 13.6	0.0368
Half-Power Bandwidth.1/2 $(\frac{f_1 - f_2}{f_1 + f_2})$	0.0331
Phase Angle, Best fit curve	0.0314
Average	0.0340

Equation (8) states that $.02\pi$ hysteretic damping would remove the
same amount of energy as .02 viscous damping. The results of the
11 node model calibration indicate that even though hystertic
damping removes the same amount of energy as viscous damping, it
does not have a comparable effect on displacements and bending
moments which are the values of interest here. From the above
results of the three methods for determining the equivalent
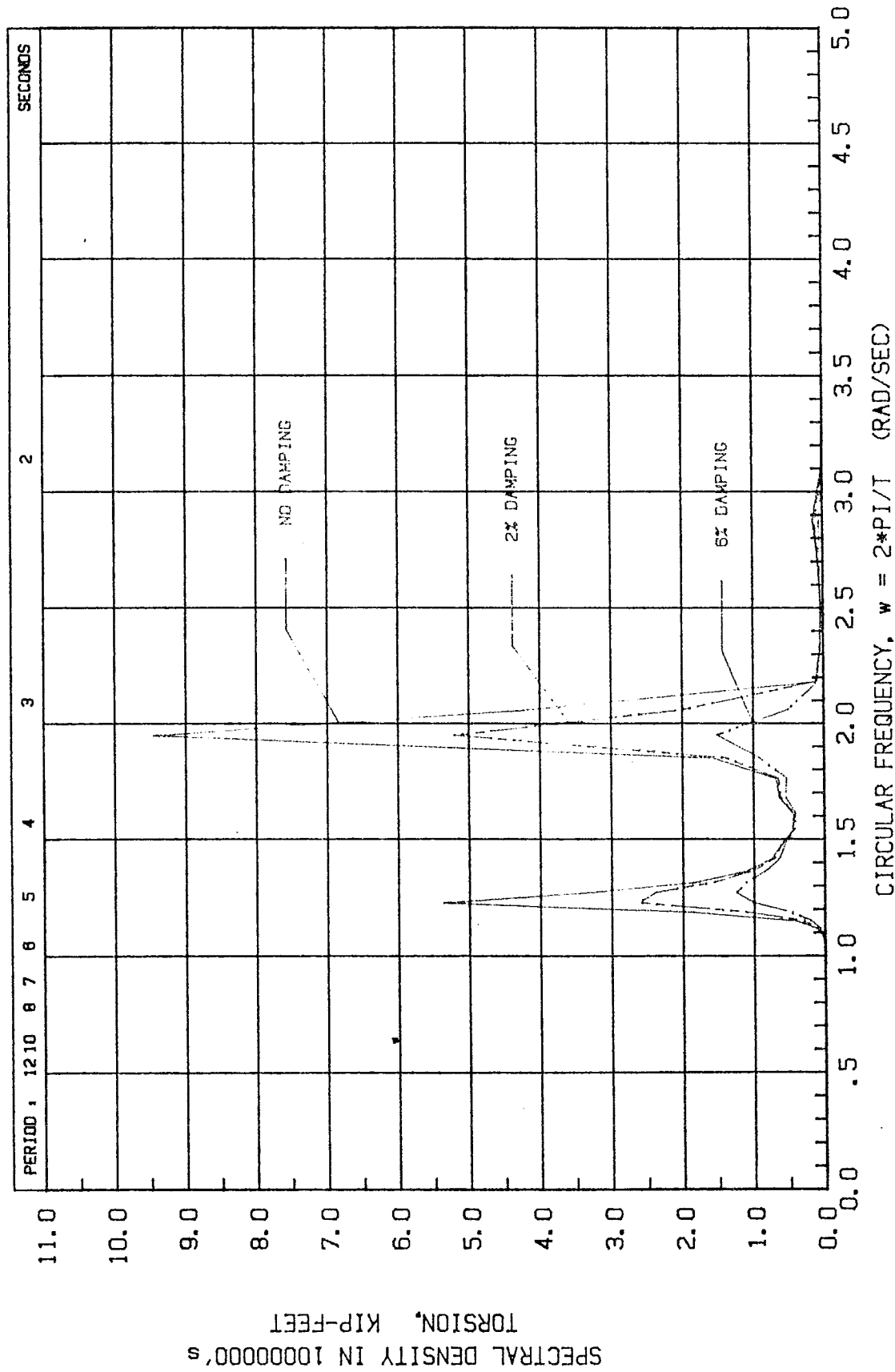viscous damping, ratio the following relationship is suggested

for comparing hysteretic damping values to published viscous values:

π x (hysteretic damping) $\simeq$ 1.85 x (equivalent viscous damping)

Please note that in subsequent volumes of this report, the final response data are labeled as having .02 or 2% hysteretic damping. In fact, these values are computed using .02π hysteretic damping, or 3.4% equivalent viscous damping.

NEW I-90 BRIDGE

PERIOD : 12 10 8 7 6 5 4 3 2 SECONDS

NO DAMPING

2% DAMPING

6% DAMPING

CIRCULAR FREQUENCY, w = 2*PI/T (RAD/SEC)

SPECTRAL DENSITY IN 10000000's
TORSION, KIP-FEET

SIG. WAVE HEIGHT = 3.37 FEET   MODAL PERIOD = 3.398 SECONDS
CENTRAL HEADING ANGLE = 90.0 DEGREES   (WIND FROM SOUTH)
COSINE-POWER SPREADING TO 12th POWER

THE GLOSTEN ASSOCIATES, inc.
13 MAY 1983

FIGURE # 15

6. HYDRODYNAMIC CHARACTERISTICS

Hydrodynamic properties are developed for each uniquely dimensioned bridge segment using strip theory, assuming two-dimensional flow conditions. Frequency dependent hydrodynamic coefficients are obtained by solving the appropriate Cauchy problem for the velocity potential using a close fit source technique first developed by Warner Frank [5] and subsequently employed by Salveson, Tuck and Faltinsen [6] in their five degree of freedom rigid body dynamics theory. Once the velocity potential is obtained for each mode of oscillation and frequency, the pressure field is obtained from the Bernoulli equation and the forces and moments are obtained by performing the contour integration of the product of the scalar pressure field and the surface inward normal unit vector on the underwater contour of the section. The algorithms we employed to perform this phase of the analysis are those embodied in the NSRDC Ship Motions and Sea Loads Computer Program [7].

We have many years of satisfactory experience using these algorithms. These algorithms are perhaps the most widely tested and confirmed algorithms for this purpose available anywhere in the world today. In addition to the many studies performed by others which have tested these algorithms, we have conducted studies of our own, including participation in an international barge-industry consortium formed to test available programs against results of a two-year testing program.

The frequency dependence of the resulting hydrodynamic coefficients reflects the influence of the fluid free surface boundary conditions on the solution of the Cauchy problem. This is of course due to the gravity waves induced at the free surface by the oscillations of the section.

The sectional wave forcing functions are also obtained from the solutions of an appropriate Cauchy problem for the velocity potential. Whereas the hydrodynamic coefficients were developed by solving the problem of the section performing small oscillations at the surface of an otherwise undisturbed fluid, the exciting forces and moments act on a stationary section subject to incident incoming waves at each frequency under examination.

7. WAVE CLIMATOLOGY MODELING

When predicting the design wave fields on Lake Washington at each
bridge site, three influential local phenomena must be forcast,
namely; wind speed, wind direction and effective fetch. Once
these phenomena are quantified they are utilized to predict
significant wave heights and periods which are in turn used as
parameters in theoretical wave spectral formulations. The
methods used in the forcasting of wave field characteristics are
presented in this volume. The results obtained at each bridge
site are contained in the appropriate subsequent volumes.

7.1 Wind Climatology

The wind speeds and directions used in our studies are based on a
revised analysis of historical data by Professor Richard J. Reed
(Appendix A to this volume) of the University of Washington.
Department of Atmospheric Science.

In his recent review of the topic Professor Reed updated an
earlier study prepared for the Lake Washington bridge sites [9]
by including consideration of recent historical wind data
covering the period since he completed his 1979 study. As there
were several notable strong wind events in recent years a slight
upward adjustment resulted in the winds projected for the site of
the new I-90 and Lacey Murrow bridges. The resulting projected
one-minute average wind speeds developed by Professor Reed are
summarized in Table 7-1 below:

Table 7-1

(One-Minute average Wind Speeds at 30 ft. Height)

Northerly Winds

Return Interval	I-90/Lacey Murrow	Evergreen Point
100 years	51 mph	38 mph
20 years	45 mph	34 mph
1 year	34 mph	25 mph

Southerly Winds

Return Interval	I-90/Lacey Murrow	Evergreen Point
100 years	63 mph	85 mph
20 years	56 mph	75 mph
1 year	43 mph	57 mph

Professor Reed also provided the ratios necessary to determine
the wind speed over averaging periods other than one-minute, in

terms of the one-minute average. This relationship indicates
that the wind speed over a six second averaging period is 25
percent greater than the one-minute average and the one-hour
average is 80 percent of the one-minute average. Ratios for
intermediate averaging periods can be read from the plot of
the relationship, included with Professor Reed's report in
Appendix A.

7.2 Wave Modeling

The effective fetch to selected nodal positions along each bridge
are calculated for various wind directions with the aid of an in-
house computer program. The calculation method utilized to
determine the effective fetch is the method of cosine-squared
weighting of radial fetch lines as described in the U. S. Army
Coastal Engineering Research Center's "Shore Protection Manual",
[10]. Our implementation of this method employed radial fetch
lines located at 5° intervals on each side of the given wind
direction, out to a maximum of 45° on either side of the wind
line.

Significant wave height was predicted from the wind speeds,
effective fetch and duration using the Servdrup, Munk,
Bretschneider (SMB) empirical equations as published in reference
[10]. The equation for significant wave height and minimum
required duration are reproduced below.

$$\frac{gH}{U^2} = 0.283 \tanh\left[0.0125\left(\frac{gF}{U^2}\right)^{0.42}\right]$$

and,

$$\frac{gt}{U} = K \exp\left\{\left(A\left(\ln\left(\frac{gF}{U^2}\right)\right)^2 - B \ln\left(\frac{gF}{U^2}\right) + C\right)^{1/2} + D \ln\left(\frac{gF}{U^2}\right)\right\}$$

where
$$\exp(x) = e^{(x)}$$
$$K = 6.5882$$
$$A = 0.0161$$
$$B = 0.3692$$
$$C = 2.2024$$

An iterative procedure was used to vary the duration until the
sea state was just fetch limited. In so doing, the wind speed
was varied according to the ratios provided by Professor Reed,
using the duration as the averaging period. This procedure
results in the greatest significant wave height obtainable from
the SMB equations for a given fetch and one-minute average wind
speed. In general the durations required to achieve a fetch
limited sea state were between 1/2 and 3/4 hours.

The hindcasting methods were tested against measured wave spectra
obtained near Sand Point as part of research being conducted by
Professor Bruce Adee of the University of Washington Department

of Mechanical Engineering. These correlation studies indicated that the effective fetch calculations described and the SMB equations could be relied upon to predict the significant wave height but that the SMB equations did not yield reasonable predictions for period.

The SMB method actually predicted significant wave heights about ten percent greater than observed. This was judged to be acceptable and accordingly no adjustment was made to the prediction of significant wave height.

The correlation of hindcast period and observed period was not so good even after adjustment was made to reconcile the archaic period definition of significant period embodied in the SMB equations with modern spectral measures of period. The observed periods correlated very well with non-dimensional fetch, with parameters falling within the bounds given in modern textbooks, such as Weigel [11]. Accordingly the following relationship was adopted to hindcast modal period (the period associated with peak wave spectral density) based on non-dimensional fetch.

$$T_O = 0.9024 \ T_S$$

where: T_O is the modal period, associated with peak spectral density

T_S is the "significant period", predicted by the modified SMB equations

The final stage of wave hindcasting is to select and confirm a spectral shape. The wave spectrum to be used was to belong to an analytical spectral family and the JONSWOP spectrum is deemed appropriate for fetch limited situations.

7.3 Coherency

The scalar coherency function as developed in reference 4 is defined analytically as:

$$\gamma_{AB}(\omega) = \int_{-\pi}^{\pi} \Psi(\theta)e^{i(\vec{k}\cdot\vec{\xi})} \, d\theta \int_{-\pi}^{\pi} \Psi(\theta)e^{-i(\vec{k}\cdot\vec{\xi})} \, d\theta \qquad (17)$$

where: $\Psi(\theta)$ is the directional spreading function satisfying the unary operator condition:

$$\int_{-\pi}^{\pi} \Psi(\theta)d\theta = 1.0$$

And $\vec{k}$ is the wave number vector

$\vec{\xi}$ is the location difference vector between field

points $\vec{A}$ and $\vec{B}$

This scalar coherency has a pair of complex conjugate roots:

$$\sqrt{\gamma_{BA}(\omega)} = \int_{-\pi}^{\pi} \psi(\theta) e^{-i(\vec{k}\cdot\vec{\xi})} d\theta$$

$$\sqrt{\gamma_{AB}(\omega)} = \int_{-\pi}^{\pi} \psi(\theta) e^{+i(\vec{k}\cdot\vec{\xi})} d\theta$$

The coherency is obviously intimately connected with the spreading function Ψ. A common analytical form for the spreading function is a cosine power function:

$$\psi(\theta) = C \cos^n(\theta-\theta_c) \quad \text{on} \quad -\frac{\pi}{2} < (\theta-\theta_c) < \frac{\pi}{2},$$

$$\psi(\theta) = 0 \qquad \text{otherwise}$$

where: C   is a constant such that the unary operator condition is satisfied

θ_c is the central heading angle

n   is positive even integer, e.g. 2, 4...

A limited quantity of scalar coherency measurements have been collected on the Evergreen Point floating bridge [12]. A reanalysis of these data was presented in reference [4]. An attempt was made to fit coherency functions derived from cosine power analytical spreading function to the reanalysed data presented in [4]. A twelfth power spreading seemed to provide a reasonable fit to the data and it was therefore that spreading function which was selected to be used throughout these bridge studies. Figure 16 shows the reanalyzed data from [4] and the bounding lines formed by the twelfth power spreading analytical coherency.

In order to evaluate the consequences of different choices of coherency a mini-parametric study was conducted to examine the effect on response statistics of varying the power of the cosine power spreading function. All wave field parameters except the power of the spreading function were held constant and the vertical bending moment over the length of the new I-90 bridge was computed for spreading powers of 2, 6, 10, 12, 14, 18 and 22. These vertical bending responses are plotted in figure 17. It may be observed that the response statistics increase with increasing power of the spreading function.
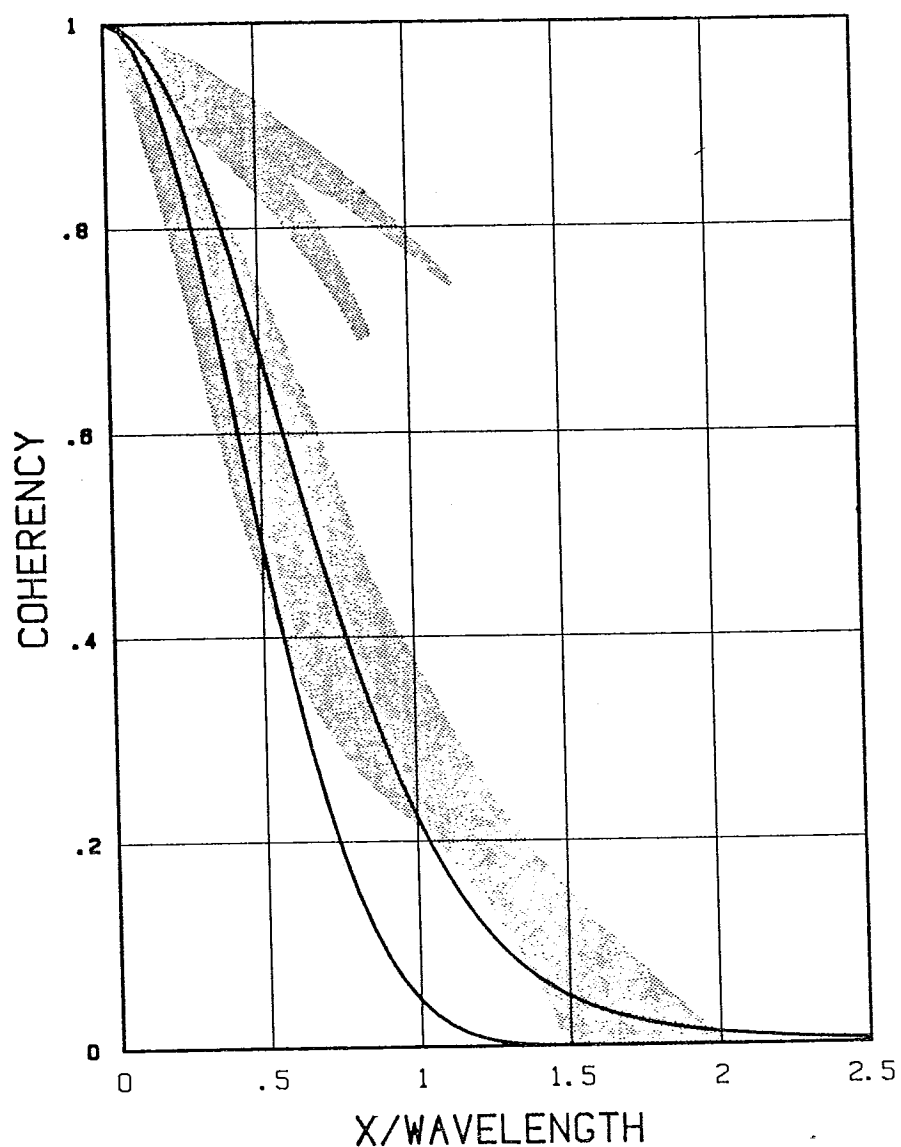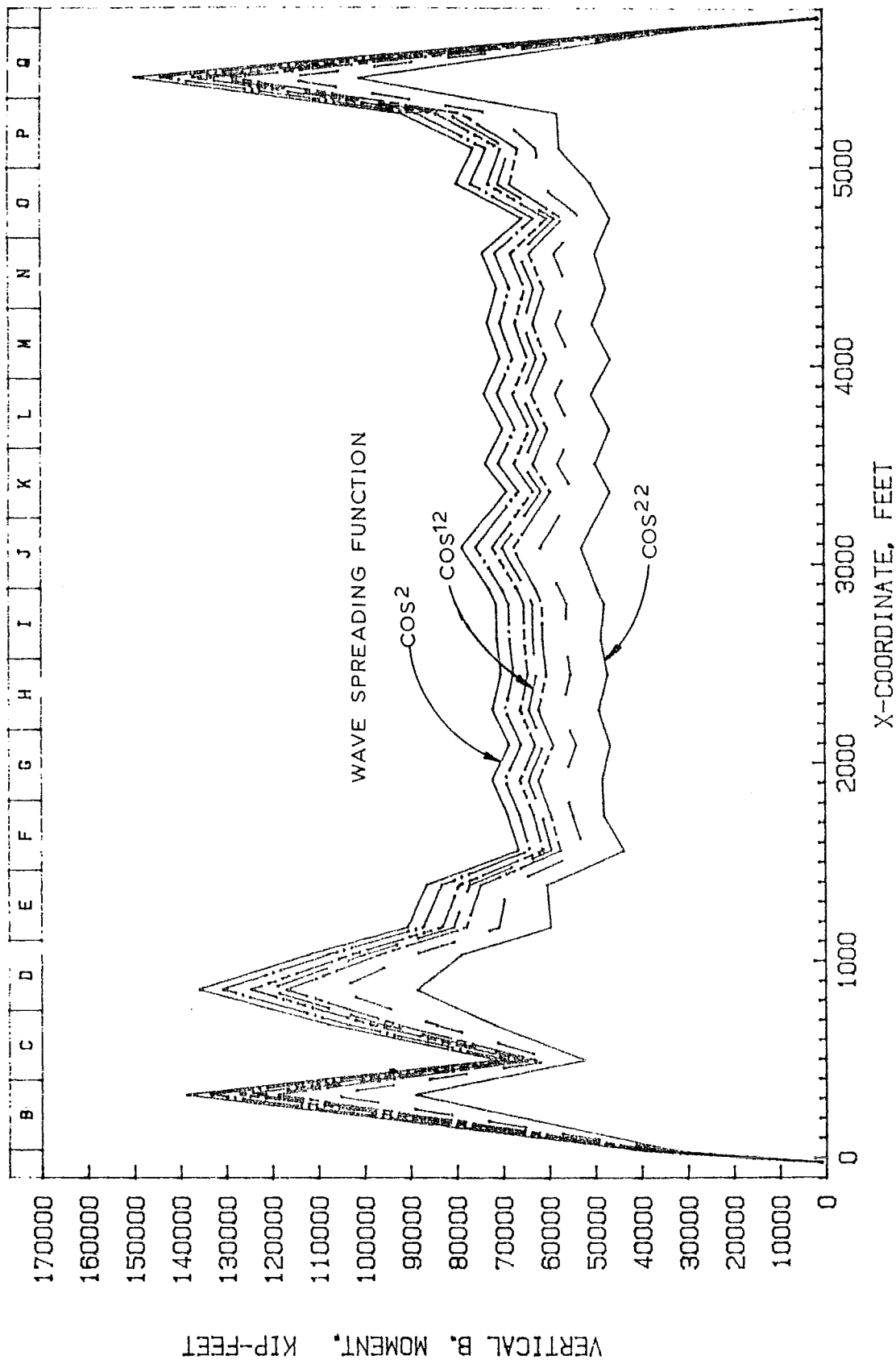
Figure 16. Shaded area shows the range of measured coherency, from reanalysis of data from [12] taken at Evergreen Point Bridge. Central heading angles ranged from 47° to 84°. Twelfth-power cosine spreading, for the bounding central heading angles, is shown by the solid lines.

NEW I-90 BRIDGE

VERTICAL B. MOMENT, KIP-FEET

X-COORDINATE, FEET

WAVE SPREADING FUNCTION

$\cos^2$

$\cos^{12}$

$\cos^{22}$

SIG. WAVE HEIGHT = 3.37 FEET   MODAL PERIOD = 3.398 SECONDS   THE GLOSTEN ASSOCIATES, inc.
CENTRAL HEADING ANGLE = 90.0 DEGREES   (WIND FROM SOUTH)   8 MAY 1983
COSINE-POWER SPREADING TO 22th POWER   FIGURE 17
HYSTERETIC STRUCTURAL DAMPING = 2%

VERTICAL MOMENT VS WAVE SPREADING FUNCTION

38

Table 7-2 gives normalization factors for vertical bending statistics with the twelth-power spreading case as a basis. Thus, if wave directional spreading followed a second cosine power the vertical bending at node 89 would be reduced to 75% of the value obtained using twelth power spreading. On the other hand, if the spreading followed a twenty-second power, the vertical bending at node 89 would be 12% greater

<div align="center">TABLE 7-2</div>

N	Node 17 δ^2_n	$\sqrt{\dfrac{\delta^2_n}{\delta^2_{12}}}$	Node 89 δ^2_n	$\sqrt{\dfrac{\delta^2_n}{\delta^2_{12}}}$
2	4.246512E+8	0.7206	1.175043E+8	0.7511
6				
10				
12	8.178283E+8	1.000	2.084314E+8	1.000
14				
18				
22	1.040463E+9	1.1279	2.638417E+8	1.1251

7.4 Effect of Heading Angle on Response

In order to evaluate the effect of the central heading angle of the directional wave spectrum (heading with respect to the bridge) on the responses of floating bridges, a mini parametric study was conducted using the analytical model of the new I-90 bridge. All wave field parameters except central heading angle were held constant with H_s = 3.37 feet, T_o = 3.396 seconds and cosine power spreading to the 12th power. Values of the central heading parameter were 90° (beam seas), 75°, 60° and 45°. Plots of structural load response statistics over the length of the bridge are shown in figures 18 through 20. These plots show that, for each of the five structural load processes considered, the loading was greatest for the beam sea case and decreased rapidly as the central heading angle departs from the 90° heading.

Based on these results it was concluded that only beam sea central heading angle cases need be examined in the analysis of the bridge responses.
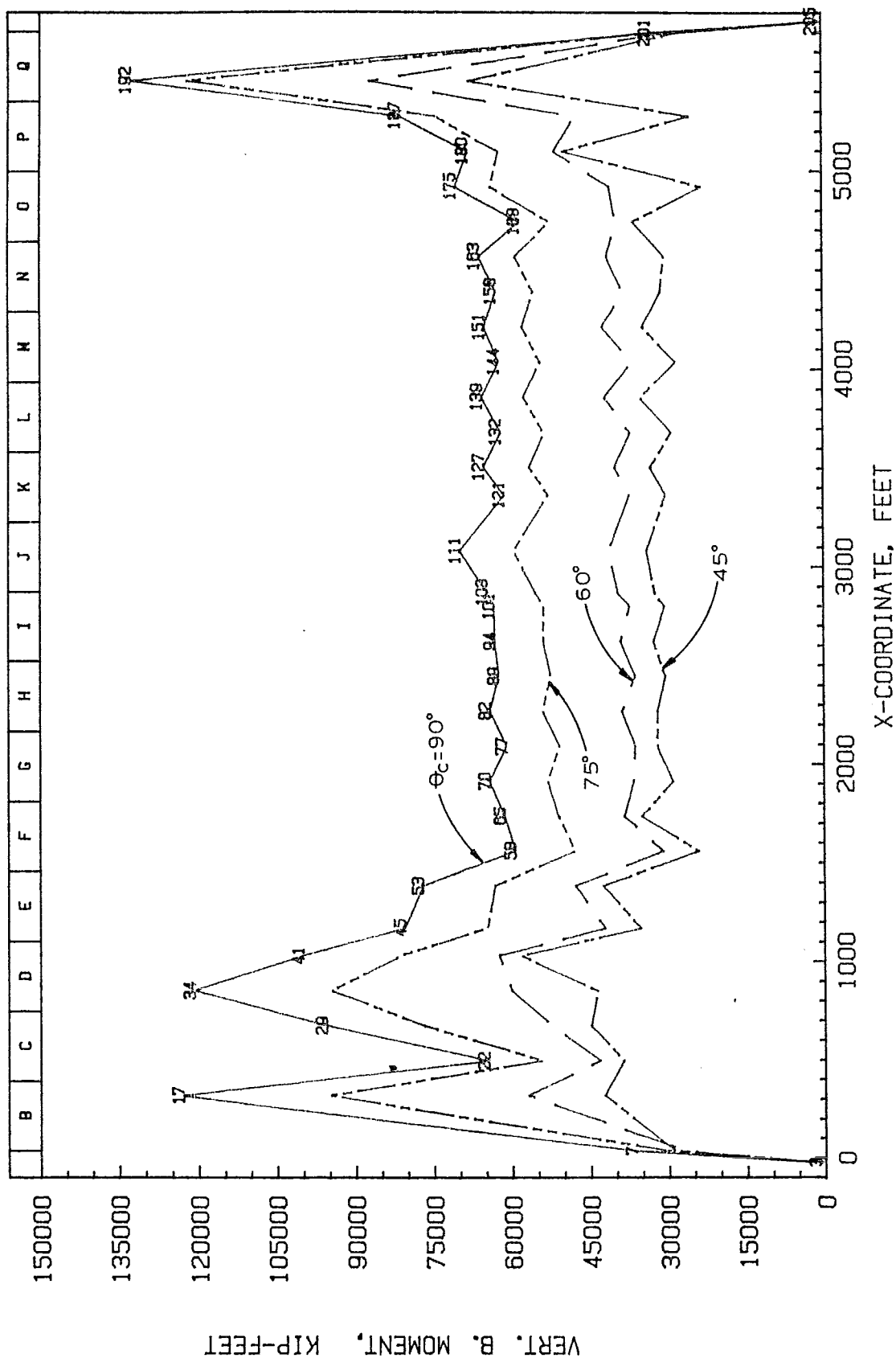
NEW I-90 BRIDGE
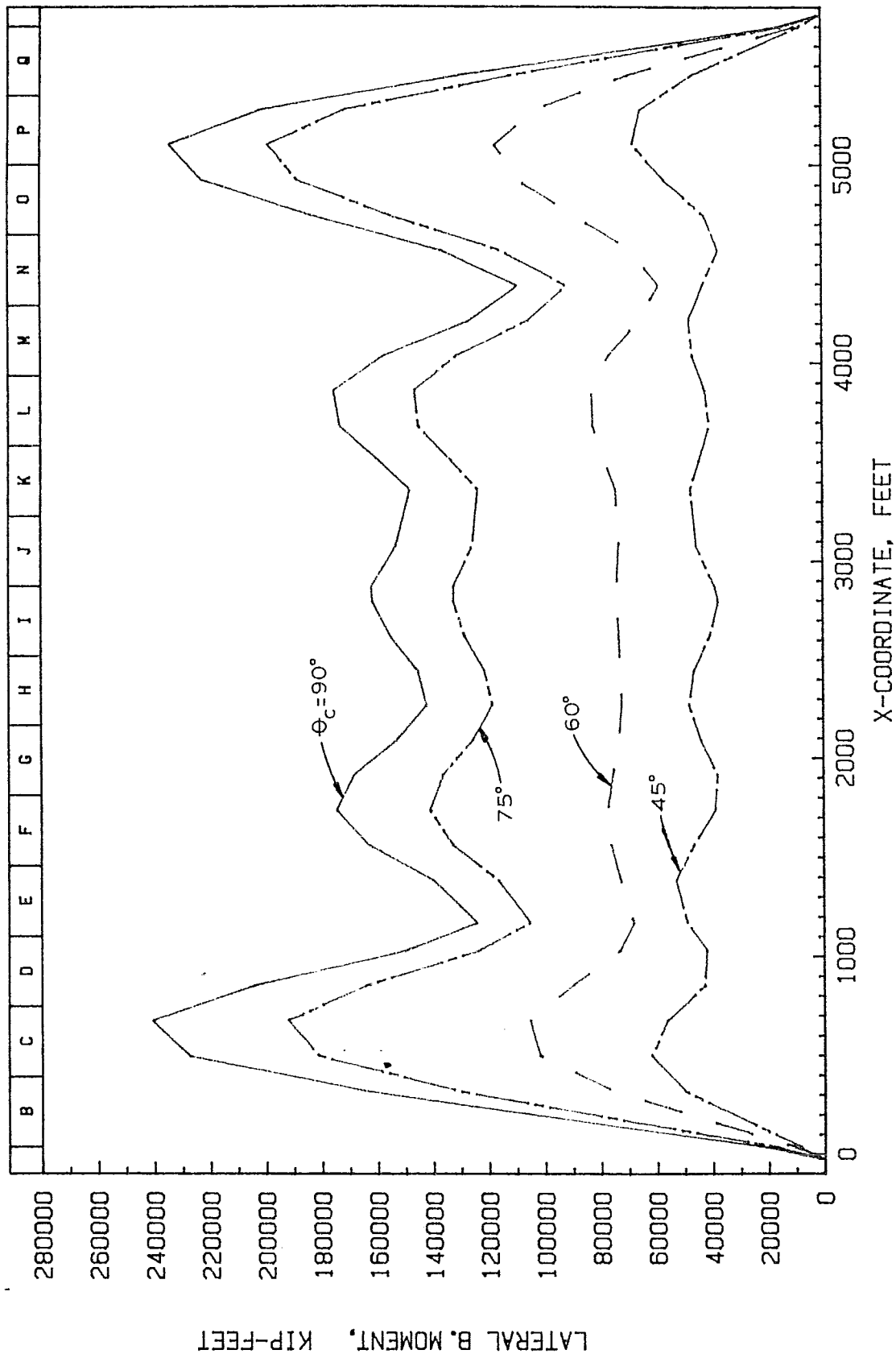
SIG. WAVE HEIGHT = 3.37 FEET   MODAL PERIOD = 3.386 SECONDS
CENTRAL HEADING ANGLE = 90.0 DEGREES   (WIND FROM SOUTH)
COSINE-POWER SPREADING TO 12th POWER
HYSTERETIC STRUCTURAL DAMPING = 2%

THE GLOSTEN ASSOCIATES, inc.
10 JUNE 1983
FIGURE 18
LATERAL MOMENT VS CENTRAL HEADING ANGLE

NEW I-90 BRIDGE

VERT. B. MOMENT, KIP-FEET

150000
135000
120000
105000
90000
75000
60000
45000
30000
15000
0

B C D E F G H I J K L M N O P Q

X-COORDINATE, FEET

0   1000   2000   3000   4000   5000

$\theta_c = 90°$

75°

60°

45°

NEW I-90 BRIDGE

TORSIONAL MOMENT, KIP-FEET

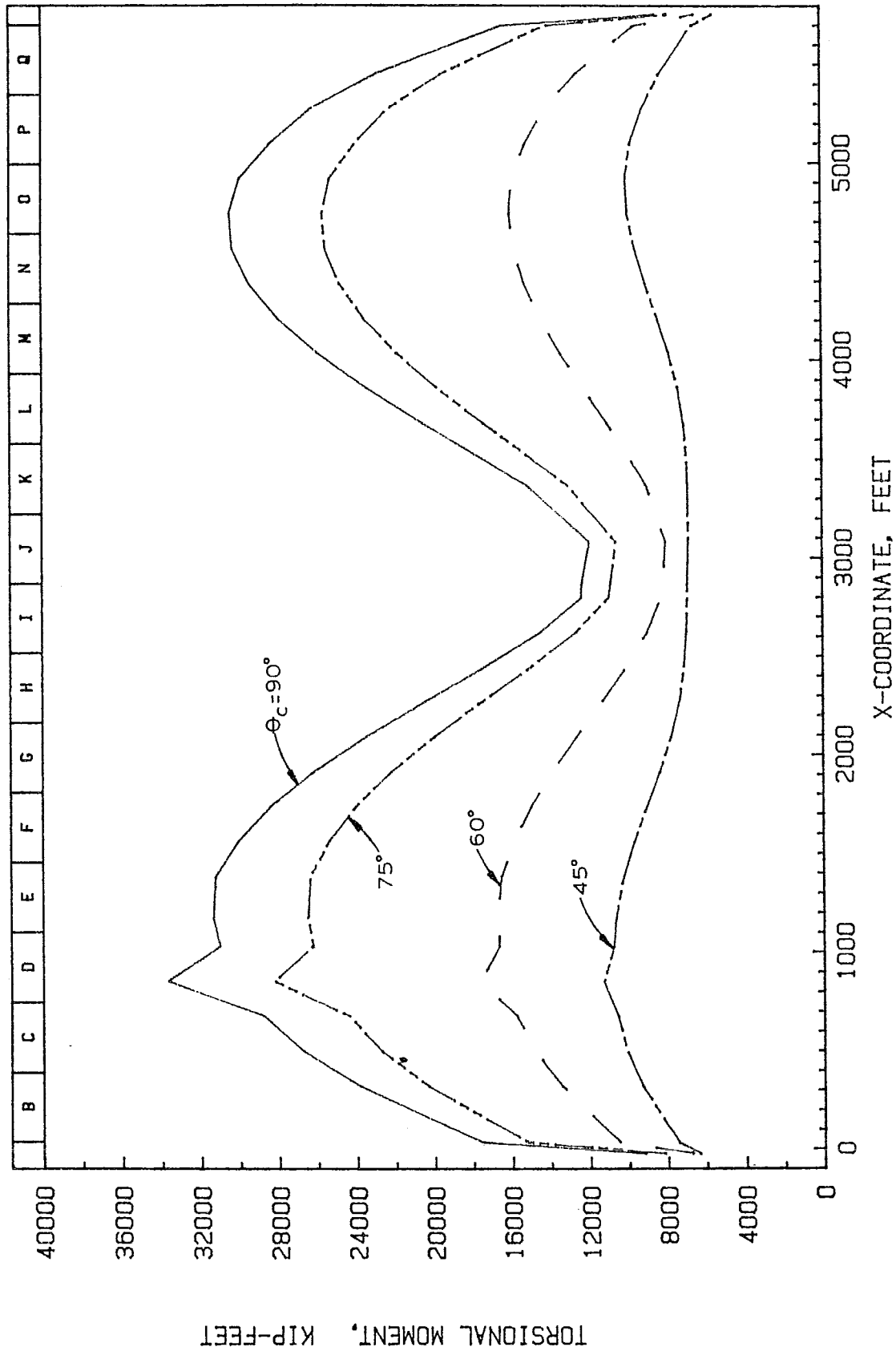X-COORDINATE, FEET

$\Theta_c = 90°$

75°

60°

45°

SIG. WAVE HEIGHT = 3.37 FEET   MODAL PERIOD = 3.386 SECONDS
CENTRAL HEADING ANGLE = 90.0 DEGREES   (WIND FROM SOUTH)
COSINE-POWER SPREADING TO 12th POWER
HYSTERETIC STRUCTURAL DAMPING = 2%

THE GLOSTEN ASSOCIATES, inc.
10 JUNE 1993
FIGURE 20
TORSION VS CENTRAL HEADING ANGLE

8. NUMERICAL PROCESSING

A flowchart of the overall numerical processing activity for the
dynamic analysis of floating bridges is shown in figure 21.
There are four major processing paths.

8.1 Hydrodynamic Data

The first two numerical processing paths develop a compatible
data base of hydrodynamic coefficients and wave forcing function
information. This data base is created using a modified version
of the NSRDC ship-motion and sea-loads computer program [8] and a
new post processor developed to produce a data base compatible
with the needs of the modified computer program FRAT.

8.2 Mass-Elastic Equation Solver

Program FRAT was modified to incorporate these hydrodynamic
inputs and solve the equations of motion (equation 1 of Section
2.3) in the complex phase-plane. Briefly, that is accomplished
as follows. Ordinary differential equation set (1) is reduced to
an algebraic equation set through substitution of a complex
amplitude vector, $\vec{x} = \vec{x}_0 e^{i\omega t}$. The resulting algebraic equation set
may be written:

$$\left([C+K] - \omega^2 \{ [M]+[A(\omega)] \} + i\{ \omega[B_1(\omega)] + [B_2] \} \right) \vec{x}_0 = \overset{=}{f} \cdot \vec{\zeta}_0$$

The impulse response analysis method requires that this equation
be solved at each ω, once for each module represented. For
purposes of discussion it is convenient to multiply the equation
above by the inverse of the response matrix on the left-hand
side, which permits writing the solution vector as:

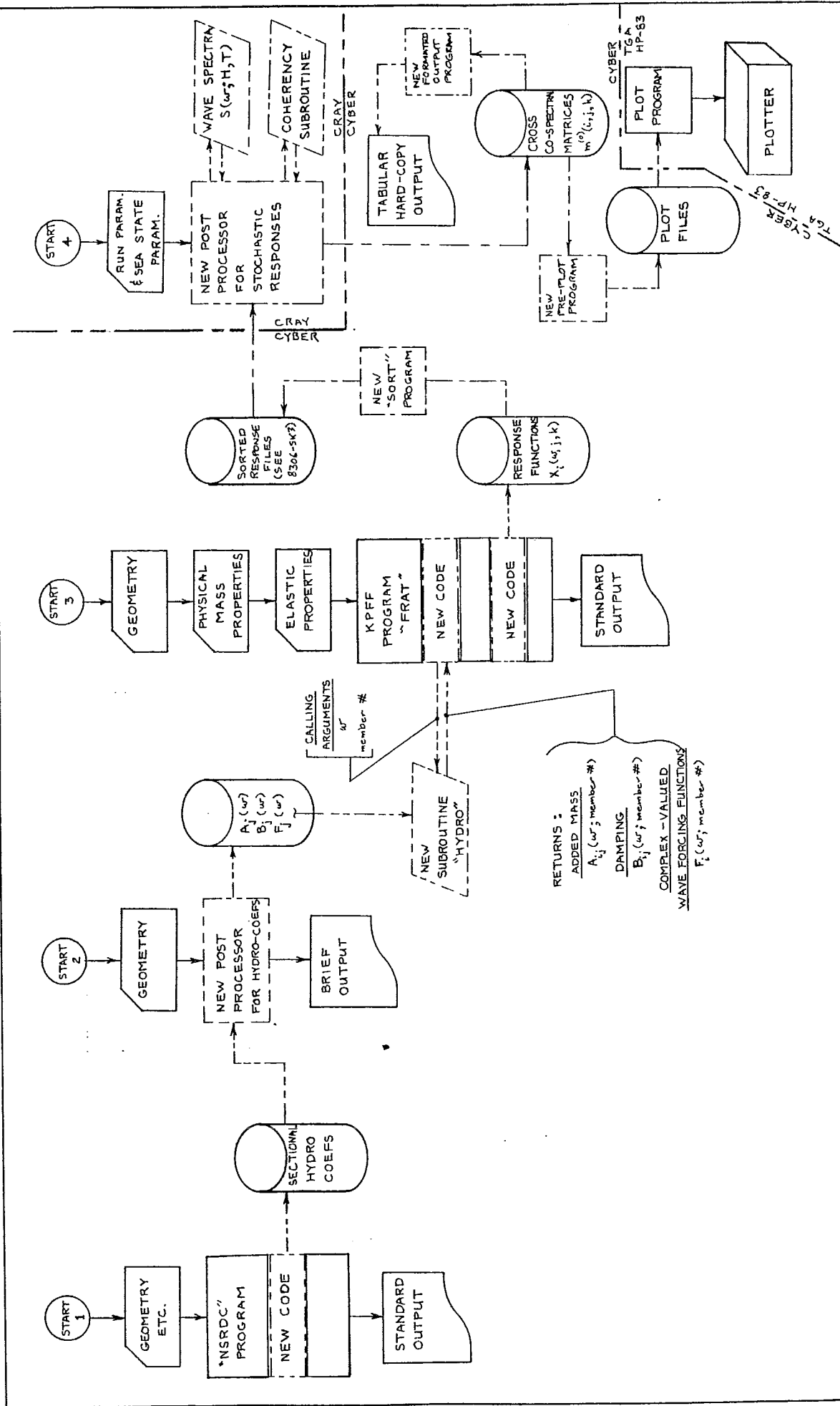$$\vec{x} = [R]^{-1} \overset{=}{f} \cdot \vec{\zeta}$$

where: $[R] = \left([C+K] - \omega^2 \{ [M] + [A(\omega)] \} + i\{ \omega[B_1(\omega)] + [B_2] \} \right)$

$\overset{=}{f}$ is the vector of wave forces and moments per unit
        wave amplitude.

$\vec{\zeta}$ is the wave amplitude vector.

This equation is evaluated with $\vec{\zeta} = \vec{\delta}(j-k)$, where $\vec{\delta}(j-k)$ is the
Dirac delta function vector (i.e. $\vec{\delta}(j-k)$ = 1 if j=k, and zero
otherwise). This evaluation is performed N-times at each ω, once
each with k=1,2,.....N. For further discussion of this segment
of the analysis the interested reader should consult reference
[4].

In this fashion the solutions with the waves acting in successive
turn on the first through the last modules are obtained. The
components of the set of solution vectors obtained in this manner
are the impulse response functions, $x_i(\omega, \frac{\pi}{2}; j, k)$.

Figure 21 — DATA PROCESSING FLOW-CHART

START 1 → GEOMETRY ETC. → "NSRDC" PROGRAM / NEW CODE → STANDARD OUTPUT

SECTIONAL HYDRO COEFS

START 2 → GEOMETRY → NEW POST PROCESSOR FOR HYDRO-COEFS → BRIEF OUTPUT

$A_j(\omega)$ $B_j(\omega)$ $F_j(\omega)$

NEW SUBROUTINE "HYDRO"

CALLING ARGUMENTS
ω
member #

RETURNS:
ADDED MASS
$A_{ij}(\omega; member \#)$
DAMPING
$B_{ij}(\omega; member \#)$
COMPLEX-VALUED
WAVE FORCING FUNCTIONS
$F_i(\omega; member \#)$

START 3 → GEOMETRY → PHYSICAL MASS PROPERTIES → ELASTIC PROPERTIES → KPFF PROGRAM "FRAT" / NEW CODE / NEW CODE → STANDARD OUTPUT

RESPONSE FUNCTIONS $X_i(\omega, j, k)$

NEW "SORT" PROGRAM

SORTED RESPONSE FILES (SEE 8306-SK7)

CRAY CYBER

START 4 → RUN PARAM. & SEA STATE PARAM. → NEW POST PROCESSOR FOR STOCHASTIC RESPONSES

WAVE SPECTRA $S(\omega; H_s, T)$

COHERENCY SUBROUTINE

CRAY CYBER

TABULAR HARD-COPY OUTPUT

NEW FORMATTED OUTPUT PROGRAM

CROSS CO-SPECTRA MATRICES $m^{(o)}(i, j, k)$

CYBER
TGA
HP-63

NEW PRE-PLOT PROGRAM

PLOT FILES

TGA
CYBER
HP-83

PLOT PROGRAM → PLOTTER

Program FRAT does not in fact invert matrix [R] but instead utilizes an LDL^T decomposition (Cholefsky decomposition) and forward/backward substitution to solve for the impulse response function.

8.3 Stochastic Post-Processor

The stochastic post-processor was developed to evaluate equation 3 (of Section 2.3) using the impulse response function data base created by program FRAT (modified). Before passing the impulse response data base to the post-processor the data base is reduced by sorting to include only impulse response functions for those nodes where response covariance is to be determined. The sorted impulse responses still retain full information concerning the effects of excitation at every node in the model, as realized at the nodes retained for final analysis.

The stochastic post-processor contains subroutines that compute the scalar wave spectral density function and the complex-valued frequency dependent coherency between each node in the analytical model. The spectral density subroutine requires as input the significant wave height and period for the sea state to be examined. The coherency subroutine requires the power of the cosine-power spreading function and the central heading angle of the incident wave spectrum. Necessary geometric information concerning node spacing is available on internal tables.

The stochastic post-processor takes advantage of the strong decay in coherency with increasing separation distance between excited nodes, by performing only a limited band-width integration on node separation distance. This was determined to be efficient and accurate in the verification activities. Certain symmetry relationships of the complex-valued covariance matrix were also exploited to obtain the greatest possible computational efficiency.
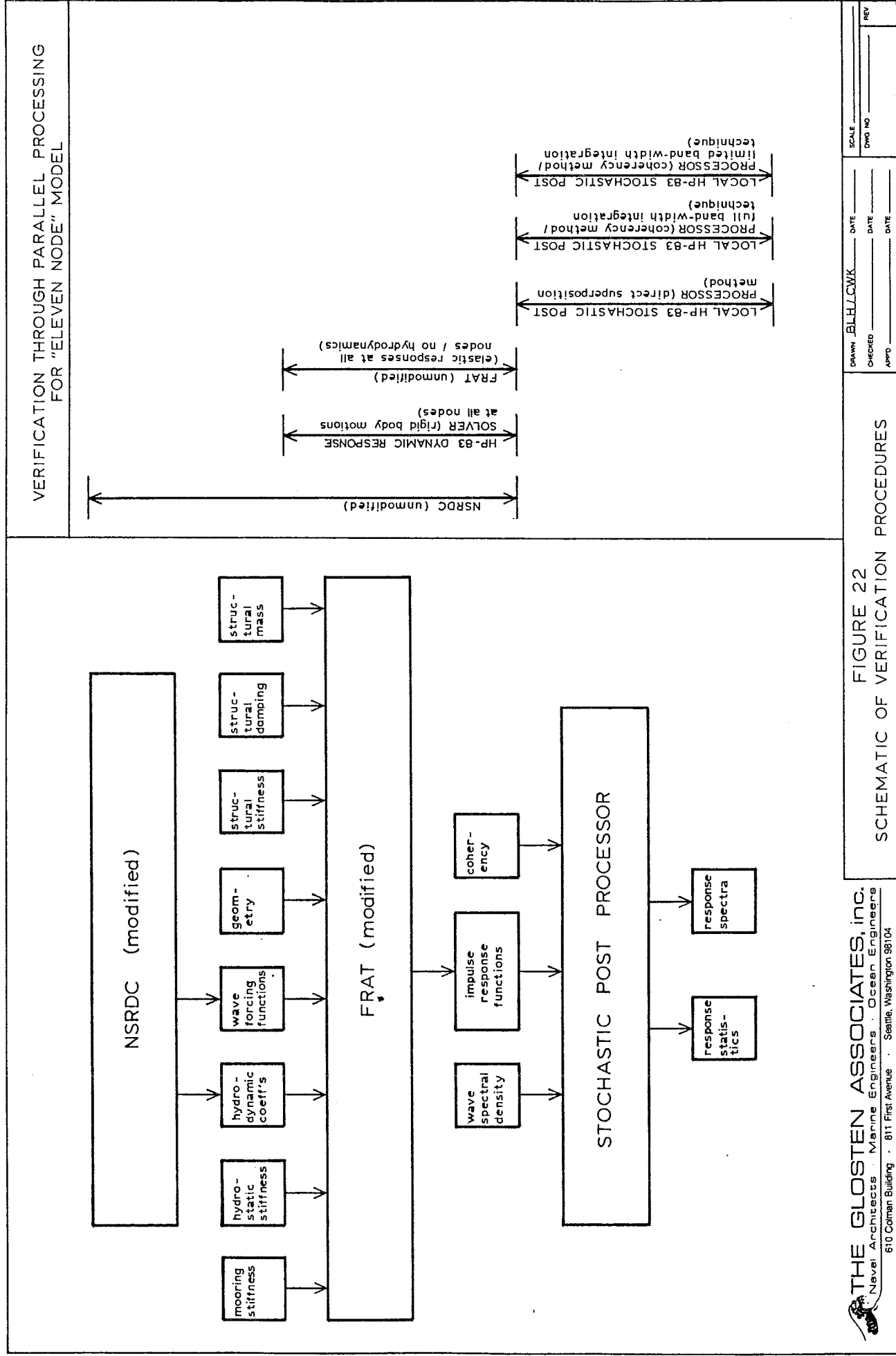
9. VERIFICATION

Verification procedures for an analytical model of the scope and complexity characterizing the subject floating bridge dynamic model, are diverse and complex in themselves. An effective strategy in building an analytical model of this scope is to utilize established and proven block elements of the largest size possible; make minimum required alterations to customize these elements to the specialized task; and verify these modified block elements, usually by running confirmation cases against the unmodified programs.

This strategy was employed in two principal blocks of the numerical processing procedure, the first being in the use of the NSRDC Ship Motions and Sea Loads computer program for hydrodynamic coefficients and wave forcing functions, and the second being in the use of KPFF'S computer program FRAT to solve the equations of motion.

A schematic presentation of these parallel verification paths is presented in figure 22. All of the parallel processing verification activity was conducted on a model of a single 353.83 foot typical pontoon from the new I-90 bridge. This verification case consisted of ten elements and eleven nodes and came to be known as the eleven node model.

The first block of parallel test cases depicted in figure 22 were utilized to verify the modifications made to program FRAT, which included introduction of hydrodynamic coefficients and wave forcing functions, and modifications to permit computation and output of impulse response functions represented in the complex phase-plane. The parallel processing contained three elements. First, the NSRDC motion was utilized to compute rigid free-body motions of the pontoon in response to long crested waves in the complex phase-plane. Second, a dynamic response solver was developed on the HP-83 which utilized as input the hydrodynamic coefficients and wave forcing functions determined by the NSRDC program. This HP-83 dynamic solver was, like the NSRDC program, a rigid-body dynamics program. However, the local HP-83 program could also compute five-degree of freedom impulse response functions for motion displacements in response to short-crested wave impulses concentrated at any node. The HP-83 dynamic solver threrfore acted as a translater between the NSRDC program and FRAT (modified). In order to permit comparison of the rigid body dynamics models with the modified version of FRAT, the structural stiffness of the eleven node model in FRAT (modified) was increased until elastic response was virtually eliminated. When this was done the impulse response solutions at all thirty frequencies for each of the five degrees of rigid body freedom agreed to five significant digits (both real and imaginary parts).

The third and final element of this block of verification was to confirm the computation of the internal loads. This was done by

VERIFICATION THROUGH PARALLEL PROCESSING
FOR "ELEVEN NODE" MODEL

NSRDC (unmodified)

HP-83 DYNAMIC RESPONSE
SOLVER (rigid body motions
at all nodes)

FRAT (unmodified)
(elastic responses at all
nodes / no hydrodynamics)

LOCAL HP-83 STOCHASTIC POST
PROCESSOR (direct superposition
method)

LOCAL HP-83 STOCHASTIC POST
PROCESSOR (coherency method /
full band-width integration
technique)

LOCAL HP-83 STOCHASTIC POST
PROCESSOR (coherency method /
limited band-width integration
technique)

NSRDC (modified)

mooring
stiffness

hydro-
static
stiffness

hydro-
dynamic
coeff's

wave
forcing
functions

geom-
etry

struc-
tural
stiffness

struc-
tural
damping

struc-
tural
mass

FRAT (modified)

coher-
ency

impulse
response
functions

wave
spectral
density

STOCHASTIC POST PROCESSOR

response
spectra

response
statis-
tics

THE GLOSTEN ASSOCIATES, inc.
Naval Architects · Marine Engineers · Ocean Engineers
610 Colman Building · 811 First Avenue · Seattle, Washington 98104

FIGURE 22
SCHEMATIC OF VERIFICATION PROCEDURES

DRAWN BLH / CWK   DATE
CHECKED   DATE
APPD   DATE

SCALE
DWG NO
REV

47

running the unmodified version of FRAT imposed with the motion solutions determined by the modified version of FRAT. The same internal loads were determined.

The second block of parallel test cases was used to verify the post processing of the impulse response functions. The approach here was to develop three different post-processors for the impulse response functions from the eleven node model. These post-processors were developed on the HP-83 computer and each implemented a different post-processing theory. Most significantly, one of the theories implemented was the direct supposition method which we had considered for the main post-processor but rejected as computationally inefficient (direct superposition is the technique utilized by several other recent teams such as Tokola/Earl & Wright and Nachlinger and Engel). The other two methods were variations on the coherency based approach also utilized in the main post-processor. The two variations were: (1) a full covariance matrix method that did not make use of the narrow bandwidth opportunities offered by the coherency function, and (2) a computationally optimized version making use of the narrow bandwidth features.

All three local programs were consistently in agreement to at least four significant digits, both in final and comparable intermediate values. All three programs also were in agreement with the main post-processing program implemented on the CRAY-1 computer at BCS. This then constituted both a verification of the main post-processing program and a numerical confirmation of the analytical proof presented in reference [4] which established the equivalence of direct superposition and coherency based methods.

It is worth observing that very substantial computing time differences were observed on the HP-83 between direct superposition and coherency based computing methods. The direct superposition technique required about fifteen times more computing time on the HP-83 than the optimized coherency based approach.

Two other elements of the overall analysis were also confirmed by independent calculation on the HP-83. These were the wave spectral density and coherency values.

Another verification activity was a brief investigation of the resolution of the integration techniques utilized in the post-processing program, when applied to damped oscillatory type functions such as were obtained. This activity was also conducted on the HP-83 and indicated that a reasonable resolution could be expected.

10. Interaction Phenomena

Two interaction phenomena are to be discussed in this section. The first is the interaction between closely spaced parallel bridges and the second is the interaction of the reflected wave field with the incident wave field. Both topics are worthy of brief investigation and discussion, but neither phenomenon has been addressed in the engineering calculations reported in subsequent volumes.

10.1 Interaction of Closely Spaced Bridges

After installation of the New I-90 bridge, the possibility will exist for fluid cavity resonance phenomena to occur in the region between the Lacey V. Murrow and New I-90 bridges. This discussion is limited to exploring the basics of this phenomenon and indicating trends and avenues for further examination.

Initially, it is advantageous to regard the surface wave phenomena which may occur between closely-spaced, stationary, parallel bridges. Later we shall comment on the possible effects of the small bridge motion responses.

The basic configuration to be considered is shown in figure 23. Typical sections of the New I-90 and Lacey V. Murrow bridges are separated by 76'-7". The discussion will proceed on the assumption that the incident wind and waves are coming from the south, and therefore first encounter the Lacey V. Murrow bridge.

Waves encountering a nearly stationary structure such as a floating bridge are partially reflected and partially transmitted. The bridge's capability to act as a break-water (and reflector) depends on the frequency of the incident waves, and a bridge may therefore be thought of as a low-pass filter for waves. A simple representation of the filter characteristics of the two bridges is shown in figure 24, in terms of transmission coefficients for wave height vs. frequency and wave length. Partial reflection coefficients can be determined from the relationship:

$$\left(\frac{H_t}{H_i}\right)^2 + \left(\frac{H_r}{H_i}\right)^2 = 1$$

where: H_i is the incident wave height

H_t is the transmitted wave height

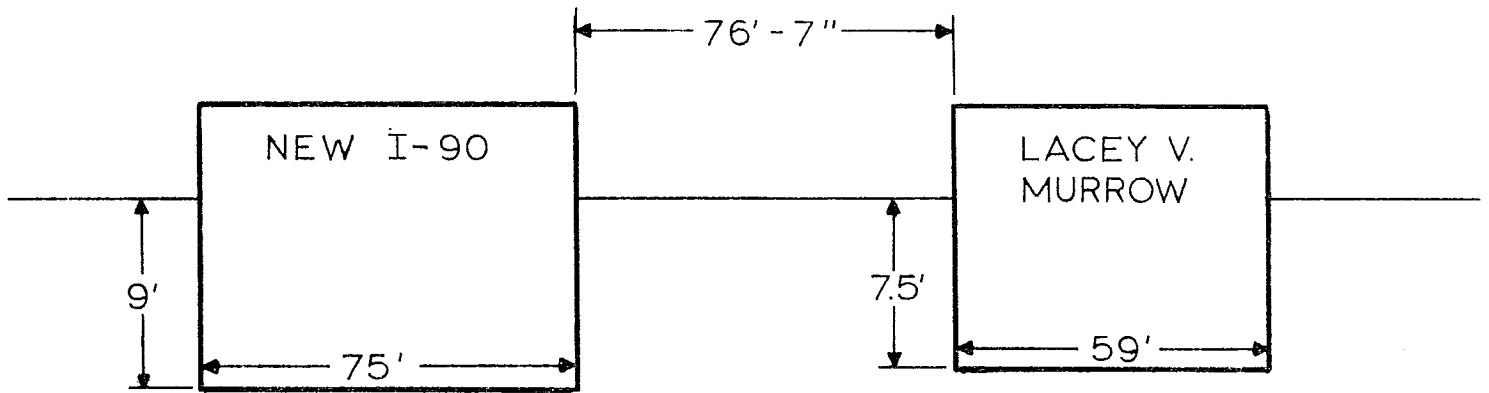That is, all wave energy is assumed to be either reflected or transmitted.

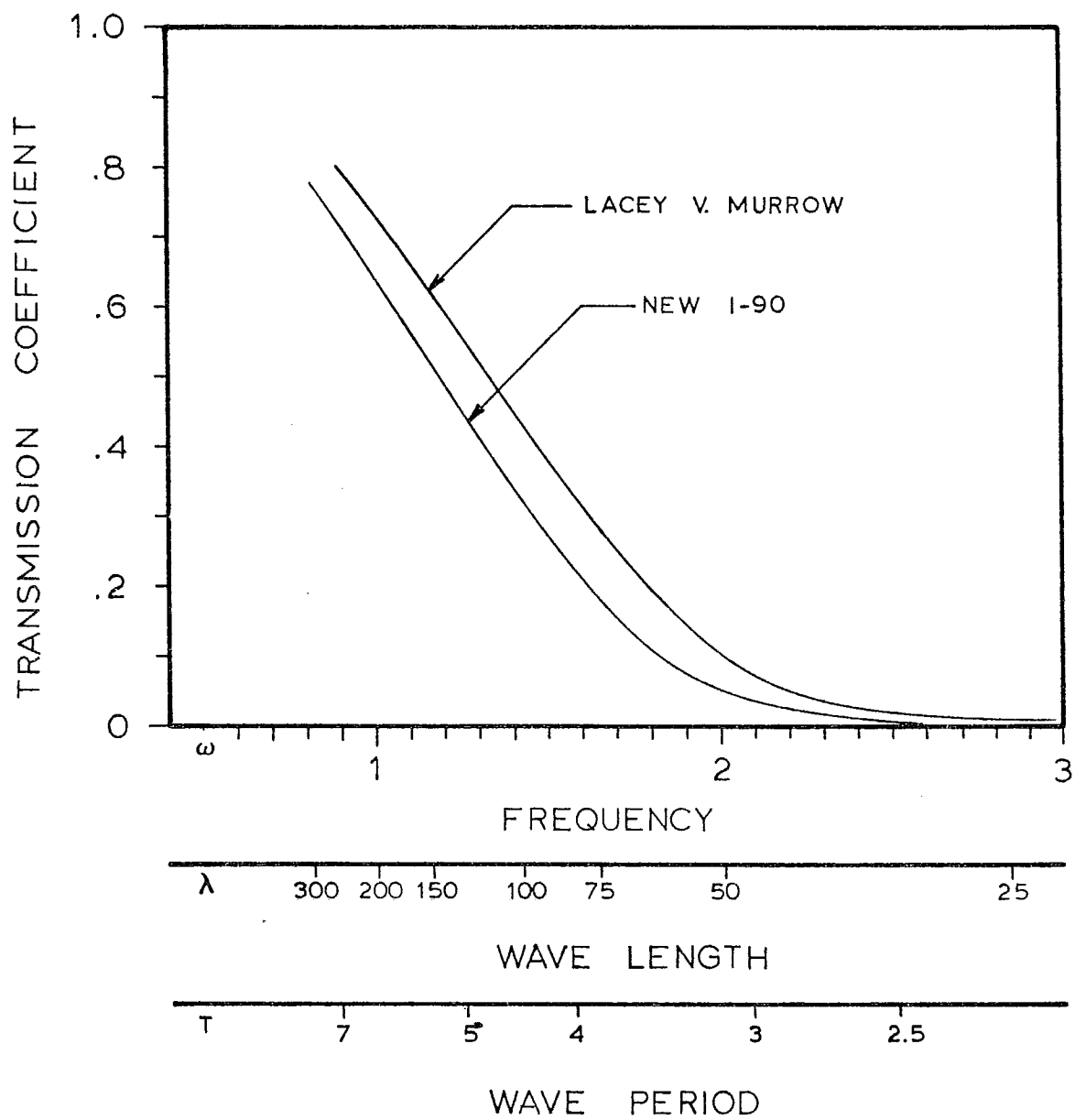FIGURE 23

THE GLOSTEN ASSOCIATES, inc.

FIGURE 24

Waves transmitted beyond the Lacey V. Murrow bridge will be partially reflected when they encounter the New I-90 bridge. At most frequencies, wave energy thus trapped in the region between bridges will be eliminated via destructive superposition processes. However, there are certain resonant modes for this region where energy will accumulate. These modes, and their associated wavelengths and periods, are illustrated in figure 25. These resonant frequencies are then the incident wave frequencies of primary interest. The transmission and reflection coefficients at each of the two bridges are tabulated in Table 10-1 for the first six cavity resonance modes.

TABLE 10-1

Transmission and Reflection Coefficients
At First Six Cavity Resonance Modes

| Resonant Mode Order | Lacey V. Murrow | | New I-90 | |
	$C_t = \dfrac{H_t}{H_i}$	$C_r = \dfrac{H_r}{H_i}$	$C_t = \dfrac{H_t}{H_i}$	$C_r = \dfrac{H_r}{H_i}$
1	0.627	0.779	0.529	0.849
2	0.296	0.955	0.195	0.981
3	0.106	0.994	0.051	0.999
4	0.035	0.999	0.013	0.9999
5	0.011	0.9999	0.005	0.99999
6	0.005	0.99999	0.002	0.999998

In the absence of any other dissipative mechanisms, incident waves at these frequencies would build a standing wave system in the region between bridges. The amplitude of the standing wave system can be obtained from the following series:

$$\left(\frac{H_s}{H_i}\right)^2 = (C_{t_1})^2 \left\{ 1 + \sum_{n=1}^{\infty} (C_{r_1})^{2(n-1)} (C_{r_2})^{2n} + \sum_{n=1}^{\infty} (C_{r_1})^{2n} (C_{r_2})^{2n} \right\}$$

where: H_s is the height of the standing wave

H_i is the height of the incident wave

$C_{t_1} = \dfrac{H_t}{H_i}$ is the transmission coefficient at the Lacey V. Murrow bridge

$C_{r_1} = \dfrac{H_r}{H_i}$ is the reflection coefficient at the Lacey V. Murrow bridge

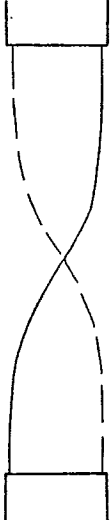$C_{r_2} = \dfrac{H_r}{H_i}$ is the reflection coefficient at the New I-90 bridge

MODE ORDER	WAVELENGTH λ	FREQUENCY ω	PERIOD τ	MODE SHAPE	STANDING WAVE RATIO $(H_s/H_i)^2$
1	153.17'	1.1488	5.469 Sec.		1.203
2	76.58	1.6247	3.867		1.406
3	51.06	1.9898	3.158		1.629
4	38.29	2.2977	2.735		1.769
5	30.63	2.5689	2.446		1.730

FIGURE 25

The standing wave coefficients are listed in the last
column of the table which forms part of figure 25.

These resonances are very sharply tuned, but some
finite value of bandwidth must be assumed, in order
to place a value on the energy which excites the
system. An electro-magnetic cavity resonance, which
is an extreme example of such a phenomenon, may have
Q values on the order of 100,000, where Q is the
ratio of the resonant frequency to the half-power
bandwidth about that resonant peak. A conservative
approach to the current problem would be to assume
that the reflection processes in our fluid cavity
problem are less perfect, thereby responding to
energy from a wider bandwidth of the incident
spectrum. Under this assumption we will pick a lower
value of Q=100

The heights of the components of the standing wave
system between bridges in the 100-year return wave
spectrum can then be estimated. A unidirectional
incident spectrum is assumed. The results for the
first five modes are presented in Table 10-2. Higher
order modes are not expected to contribute
significantly to the final results.

TABLE 10-2

Mode Order	Resonant Frequency	$\left(\dfrac{H_s}{H_i}\right)^2$	Wave Spectral Density $S(\omega)$	Bandwidth $\Delta\omega$	Standing Wave Height, H_s
1	1.1488	1.203	0.0033	0.0115	0.0136 ft.
2	1.6247	1.406	0.3874	0.0162	0.1881
3	1.9898	1.629	0.7927	0.0199	0.3206
4	2.2977	1.769	0.2580	0.0230	0.2048
5	2.5689	1.730	0.1724	0.0257	0.1751

Even assuming phasing resulting in maximum reinforcement, the
maximum double amplitude of the standing wave system in the
region between bridges would be less than one foot.

The small motion responses of the bridges will also produce
regenerated waves on the leeward side of the Lacey V. Murrow
Bridge. Destructive superposition will again eliminate most
of these, except at the resonant modes. The effect of the
superposition of these regenerated waves on the standing wave
system due to transmitted wave energy will depend on the
phase relationships. However, the regenerated waves are
expected to be small in any case.

54

The ultimate effects of the cavity resonance on bridge responses is not expected to be great. Again it will depend on the phasing whether the effect is to increase or decrease loading. If a coherent set of parallel crested standing waves were developed between the bridges, the principal effect would most likely be to excite the rigid-body sway motions of the bridges. The greatest structural impact would then be on the mooring lines.

10.2 Interaction of Reflected and Incident Wave Fields

As the reflected waves on the weather side of a floating bridge progress upwind through the incident wave field a region of steep breaking waves is created in the vicinity of the bridge. This region is quite noticeable to an observer even during periods of moderate wave activity. The wave energy scattered during the breaking process represents energy removed from the wave system. A portion of the scattered wave energy presumably originates from the incident wave field. Thus it is implied that floating bridges impose, through the reflected wave process, a sort of protective field that tends to limit the incident progressive wave energy that can penetrate to the bridge itself. The stronger the incident wave field, the stronger is the protective reflected wave field extended upwind of the bridge. This action is reminiscent of the operation of a chemical buffer solution.

Figure 26 is a schematic illustration of this process showing the modification of far field incident wave energy H_∞ by the reflected wave energy H_r encountered in the interaction zone. By way of example, consider the following incident wave problem:
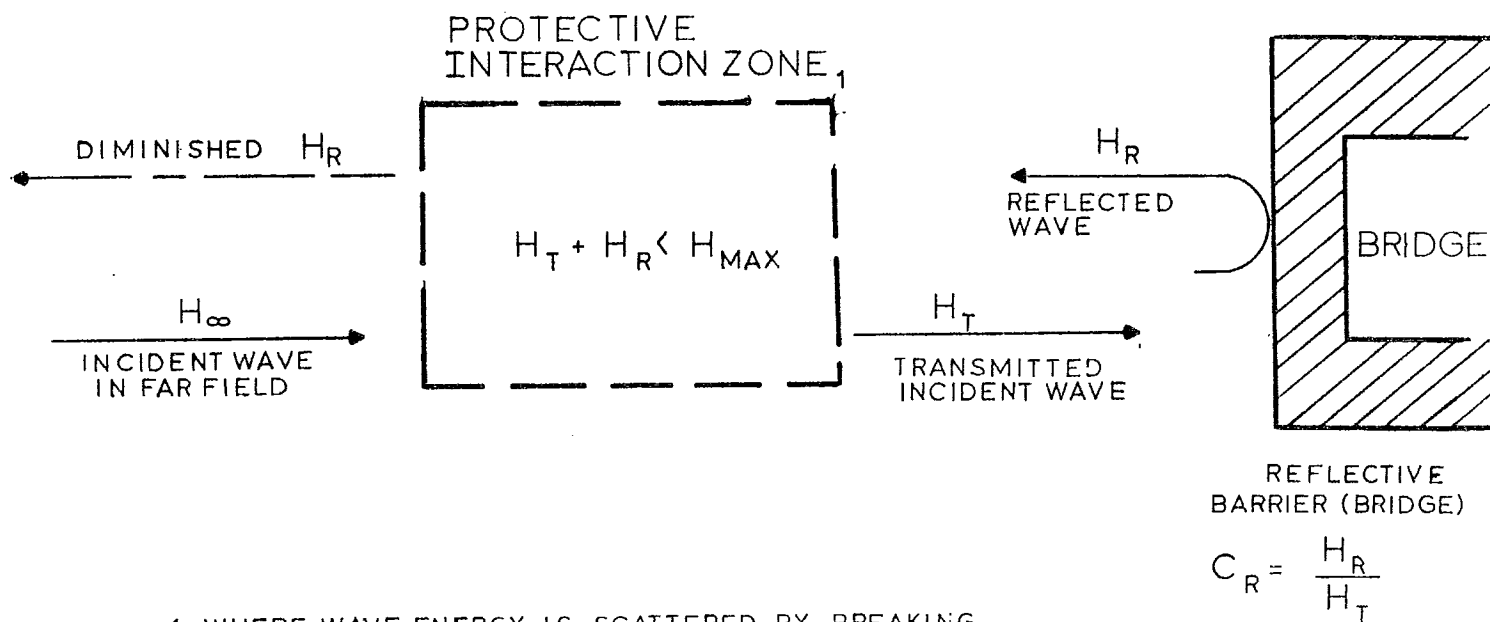
Far Field Incident Wave:

$T = 2$ seconds, $\omega = \pi$
$\lambda = 20.48$ feet

Breaking Wave Limit (Stokes):

$$H_{max} \leq \frac{\lambda}{7} = 2.93 \text{ feet}$$

Reflection Characteristics (Lacey V. Murrow):

$$\left(\frac{H_r}{H_i}\right) = C_r \simeq 0.9987$$

PROTECTIVE
INTERACTION ZONE [1]

DIMINISHED H_R

$H_T + H_R < H_{MAX}$

H_∞
INCIDENT WAVE
IN FAR FIELD

H_T
TRANSMITTED
INCIDENT WAVE

H_R
REFLECTED
WAVE

BRIDGE

REFLECTIVE
BARRIER (BRIDGE)

$$C_R = \frac{H_R}{H_T}$$

1 WHERE WAVE ENERGY IS SCATTERED BY BREAKING

FIGURE 26

The wave height transmitted through the interaction field will be limited by:

$$H_t + H_r = H_t(1+0.9987) \leq 2.93 \text{ feet}$$

Therefore:

$$H_t \leq 1.46 \text{ feet}$$

Far field incident waves greater than 1.46 feet will always be reduced in height by the protective field, to a transmitted wave height no greater than 1.46 as shown in the following table:

Table 10-3

T = 2 Seconds λ = 20.48 feet

H_∞	H_t	H_r	$(H_t + H_r)$	(H_t/H_∞)
0.5 ft.	0.50 ft.	0.50 ft.	1.00 ft	1.00 ft
1.0	1.00	1.00	2.00	1.00
1.5	1.46	1.46	2.93	0.97
2.0	1.46	1.46	2.93	0.73
2.5	1.46	1.46	2.93	0.58
2.93	1.46	1.46	2.93	0.50

Where the incident wave field is derived from an irregular wave spectrum the processes are more complex and less easily understood. In addition to energy dissipation between incident and reflected waves of like frequency, there will be breaking interactions between incident and reflected waves of dissimilar frequencies. What is obvious, however, is that a significant energy dissipation process is at work. In the case of the irregular wave spectrum the anticipated effect would be to reduce the amplitude of the wave spectral energy transmitted through the interaction zone. The frequency range most effected would presumably be the higher frequencies, occuring to the right of the spectral peak.

This interaction phenomenon in the wave field upwind of floating bridges should have a measurable effect of reducing actual bridge responses to values less than predicted by linear theory. No such reductions have been included in the engineering analyses of the subject bridges, as this would be both non-conservative and beyond the current, proven state-of-the-art. But examination of these dissipative processes would be a subject worthy of further acedemic inquiry.

REFERENCES

1. Pierson, W. J., Jr., "A Unified Mathematical Theory for the Analysis, Propagation and Refraction of Storm Generated Ocean Surface Waves," Parts I and II, NYU, Coll. of Eng. Res. Div., Dept. of Meterol. and Oceangr. Prepared for the Beach Erosion Board, Department of the Army, and Office of Naval Research, Department of the Navy, 1952.

2. Hartz, B. J. "Summary Report on Structural Behavior of Floating Bridges," for The Washington State Department of Highways, Contract Y-909, Department of Civil Engineering, University of Washington, June 1972.

3. Mukherji, Basuder, "Dynamic Behavior of a Continuous Floating Bridge," PhD. Dissertation, University of Washington, 1972.

4. Hutchison, Bruce L., "Impulse Response Techniques for Floating Bridges and Breakwaters Subject to Short-Crested Seas," Presented to Pacific N.W. Section SNAME, 23 October 1982.

5. Ochi, Michel K., "On Prediction of Extreme Values," Journal of Ship Research, March 1973.

6. Frank, W., "Oscillation of Cylinder In or Below the Free Surface of Deep Fluids," NSRDC Report 2357 (1967).

7. Salvesen, N., E. O. Tuck, and O. Faltinsen, "Ship Motions and Sea Loads," SNAME Transactions, Vol. 78, pp 250-287 (1970).

8. Meyers, W. G., Sheridan, D. J. and Salvesen, N. "NSRDC Ship Motion and Sea-Load Computrer Program," NSRDC Report 3376, Feb., 1975.

10. Shore Protection Manual, Volume I, U. S. Army Coastal Engineering Research Center, 1977.

11. Wiegel, Robert L., Oceanographical Engineering Prentice-Hall, Englewood Cliifs, N.J. (1964).

12. Seltzer, G. H., "Wave Crests-How Long?" University of Washington, Department of Civil Engineering, October 1979.

13. Hutchison, B. L., and Bringloe, J. T. "Application of Seakeeping Analysis," Marine Technology, October 1978.

14. Ochi, Michel K., "Principles of Extreme Value Statistics and their Application," Extreme Loads Response Symposium, The Ship Structure Committee and The Society of Naval Architects and Marine Engineers, October 19-20, 1981, Arlington, Virginia.

15. Clough, Ray W., <u>Dynamics of Structures</u>, McGraw-Hill, Inc., 1975.

APPENDIX A

Professor Richard J. Reed
Department of Atmospheric Sciences, AK-40
University of Washington
Seattle, Washington 98195
(206) 543 4575

March 11, 1983

J. Thomas Bringloe
The Glosten Associates, Inc.
610 Colman Building
811 First Avenue
Seattle, Washington 98104

Dear Mr. Bringloe,

This letter report is in reply to your request of 7 February 1983 for
meteorological data that can be used in developing extreme wave climatology
at the site of the new I-90 Lake Washington bridge, as well as at the two
existing bridge sites. As discussed in our earlier conversations, only two
sets of wind records are available that are suitable for estimating extreme
winds on Lake Washington. These are measurements made by the Washington
State Department of Transportation at the tower on the Evergreen Point Bridge
and by the National Weather Service at the Seattle-Tacoma Airport, located
10 miles to the south-southwest of the I-90 bridge site.

Data from these locations for the years 1970-1979 at the bridge and
1954-1979 at the airport were used in a previous study of extreme winds,
which I carried out on behalf of Tokola Offshore, Inc. The results of this
study are contained in my letter of 14 December 1979 to Mr. John Darby,
a copy of which is in your possession.

In view of the additional strong wind episodes that have occurred during
the past few years it was deemed advisable to update the earlier extreme value
analysis. This has been possible only in part, since the logs from which
data on extreme northerly winds at the bridge site were extracted were discon-
tinued in June 1980. Strong south wind events, however, can be documented for
the intervening years. Moreover, in the limited time available it was not pos-
sible to obtain additional data on extreme northerly winds at the airport.
These shortcomings are not believed to be serious in view of the generally
weaker strength of the northerly winds and their lesser importance relative to
winds from southerly directions.

The attached figures show the new estimates of return periods for
one-minute extreme north and south winds at the Lacey Murrow, or I-90, bridge
location (Fig. 1), the Seattle-Tacoma Airport (Fig. 2) and the Evergreen
Point bridge (Fig. 3). For reasons stated above, the north wind estimates
for the airport and the Evergreen Point bridge have not been revised and
appear as in the earlier report. The new estimates for southerly winds at the
airport, Evergreen Point bridge and I-90 bridge site (based as before on
Seattle-Tacoma Airport winds corrected upward by 6 percent to allow for the
overwater fetch) are little changed from the previous estimates as a result
of the data additions.

The largest change shown is for northerly winds at the I-90 bridge site. The revised curve in Fig. 1 is based on new information provided by Mr. Garcia, the bridge superintendent, who stated that on one occasion a hand-held anemometer was used to compare northerly winds at the two bridge sites. On this occasion, believed typical by the bridge superintendent, a 33 mph wind speed at Evergreen Point corresponded to a 43-45 mph wind speed at Lacey Murrow. This suggests an upward correction of 33 percent for estimating winds at the latter site from those at the former, rather than the 10 percent figure used in the previous study. Accordingly the 33 percent figure has been employed in constructing the line labeled "north" in Figure 1.

Based on the new graphs, the one-minute wind speed equalled or exceeded once in 100 years for northerly and southerly winds at the two bridge locations are:

	Northerly	Southerly
I-90/Lacey Murrow	51 mph	63 mph
Evergreen Point	38 mph	85 mph

In your request for meteorological information, you also asked for half-hourly and one-hourly wind speeds that correspond to the one-minute values. These can be obtained from the graph shown in Fig. 4. This graph is based on measurements taken at the Hood Canal Bridge. The data are tabulated in "Hood Canal Floating Bridge Study, Phase II, Report on Recommendations for Replacement Structure" WSDOT, October 1970. In my view the Hood Canal data are valid for the Lake Washington area.

You also have requested information regarding wind gradients along Lake Washington, in particular how southerly winds increase in blowing from the south end of the lake to the Mercer Island bridge and from there to the Evergreen Point Bridge and how north winds increase in blowing from the north shore to the Evergreen Point bridge and from there to the Mercer Island bridge. Since wind measurements are available for only one site on Lake Washington, it is very difficult to provide this information. Theoretical studies of wind changes over water bodies or in going from land to water are of no help inasmuch as they cannot be applied in a region of complex terrain such as the lake and its surrounding hills. Channeling and sheltering effects that are peculiar to the location greatly influence the wind behavior.

There is evidence that such effects are present over and in the vicinity of the lake, if the bridge superintendent's estimates of relative speeds at the two bridges are to be believed. The 33 percent increase in the northerly wind speed between the Evergreen Point bridge and the Lacey Murrow bridge far exceeds the expected increase of a simple land/water configuration. The bridge superintendent also claims that southerly winds increase by 30-40 percent in travelling from the Lacey Murrow bridge to the Evergreen Point bridge. This too is in conflict with a simple theoretical model, and, in addition, requires that south winds at the Lacey Murrow bridge and at Seattle-Tacoma

airport be of about equal force despite the overwater fetch upwind of the bridge. This relationship, too, is contrary to expectations.
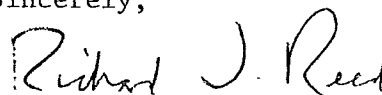
In view of the many uncertainties regarding wind gradients, I suggest that the following simple procedure be employed in specifying wind changes along the lake:

(1) In treating cases of southerly winds, use the lines labeled "south" in Figs. 1-3, assuming that the Seattle-Tacoma curve applies at the south shore and that variations are linear between the three locations. Thus, for example, a south wind of 25-year return period increases from 54 mph at the south end of the lake to 57 mph at the Lacey Murrow bridge to 76 mph at the Evergreen Point bridge.

(2) For northerly winds assume that winds are 33 percent less in the immediate vicinity of the Kenmore Air Harbor than at the Evergreen Point bridge. This figure is based on a subjective estimate provided by an experienced pilot at the airport. Beginning at a point one-half mile to the south, assume that the wind increases linearly from there to the Evergreen Point bridge, where the curve labeled "north" in Fig. 3 can be applied, and, again, linearly from that bridge to the Lacey Murrow bridge, where the curve labeled "north" in Fig. 1 is applicable.

I hope the foregoing information is of help to you in developing extreme wave climatology. If I can be of further help, do not hesitate to call.

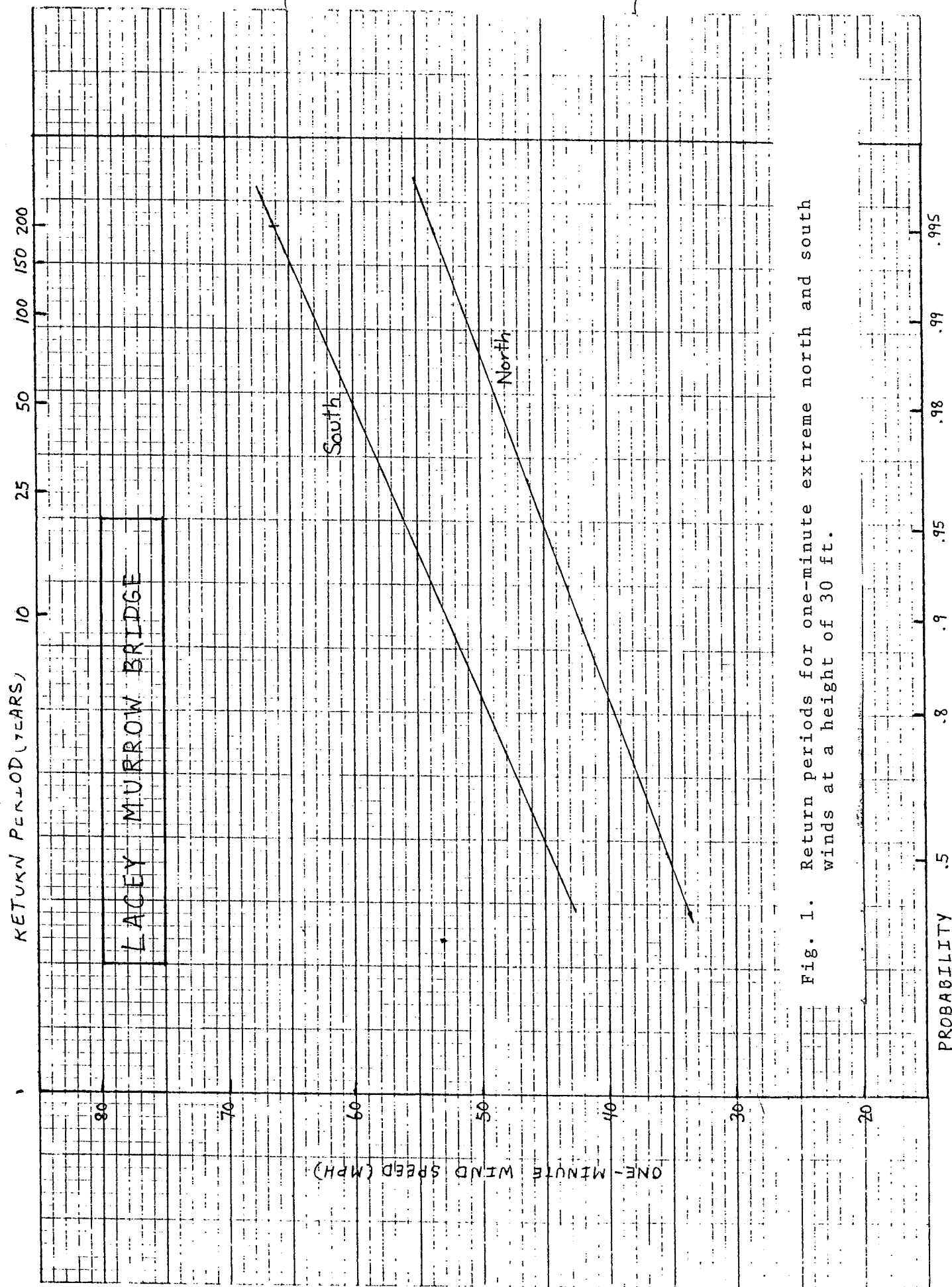Sincerely,

Richard J. Reed
Professor

RJR:KS

Fig. 1.   Return periods for one-minute extreme north and south winds at a height of 30 ft.

PROBABILITY

RETURN PERIOD (YEARS)

LACEY MURROW BRIDGE

South

North
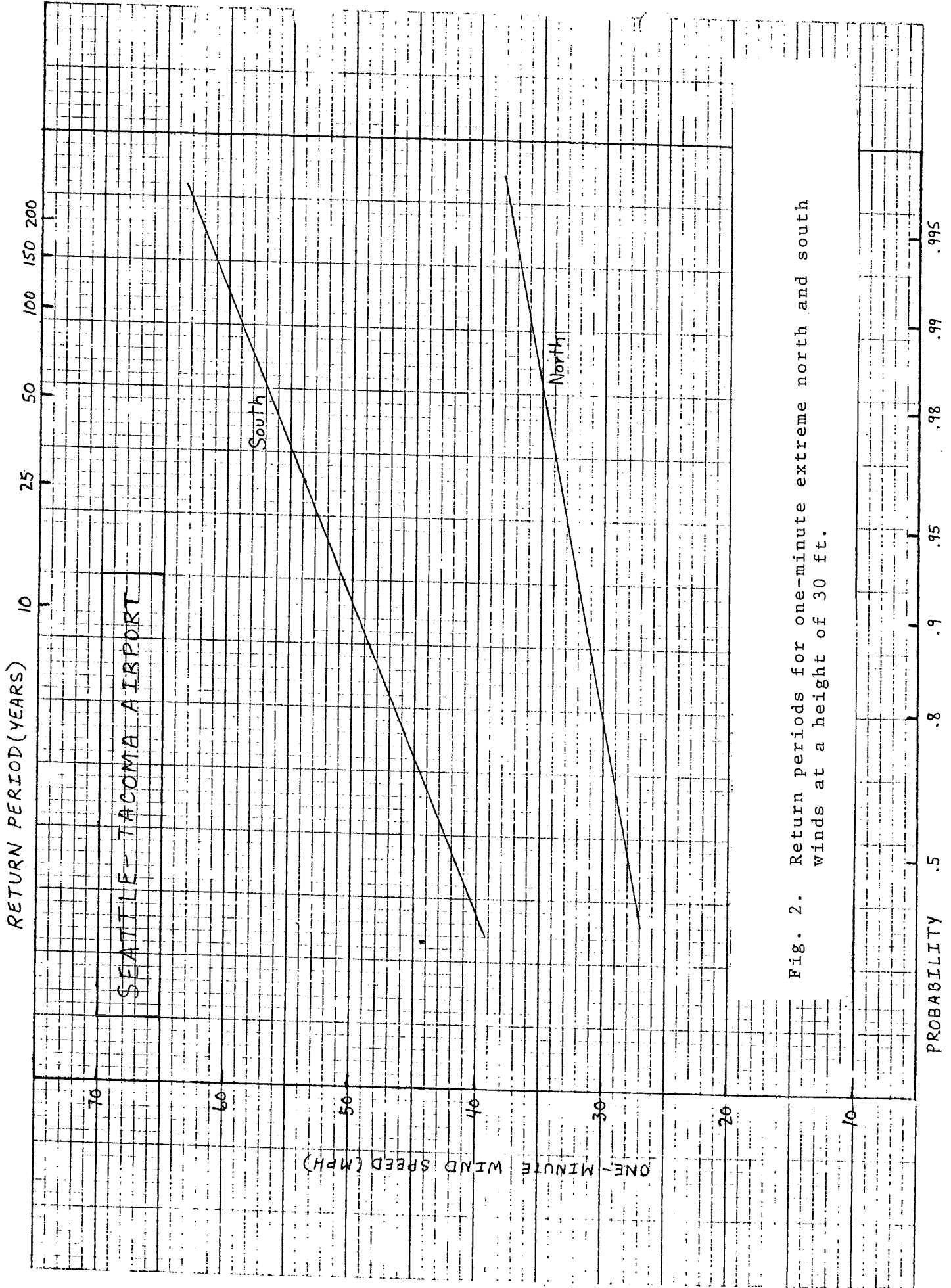
ONE-MINUTE WIND SPEED (MPH)

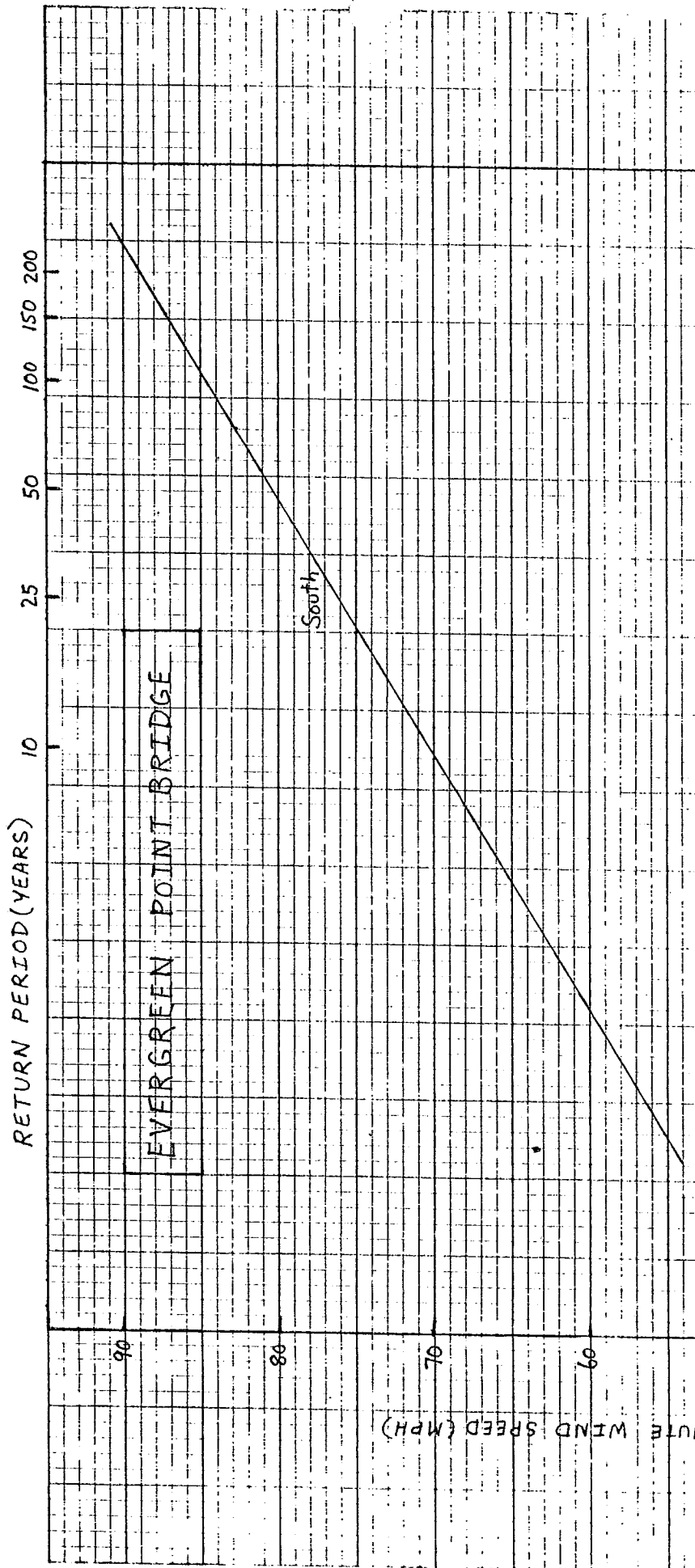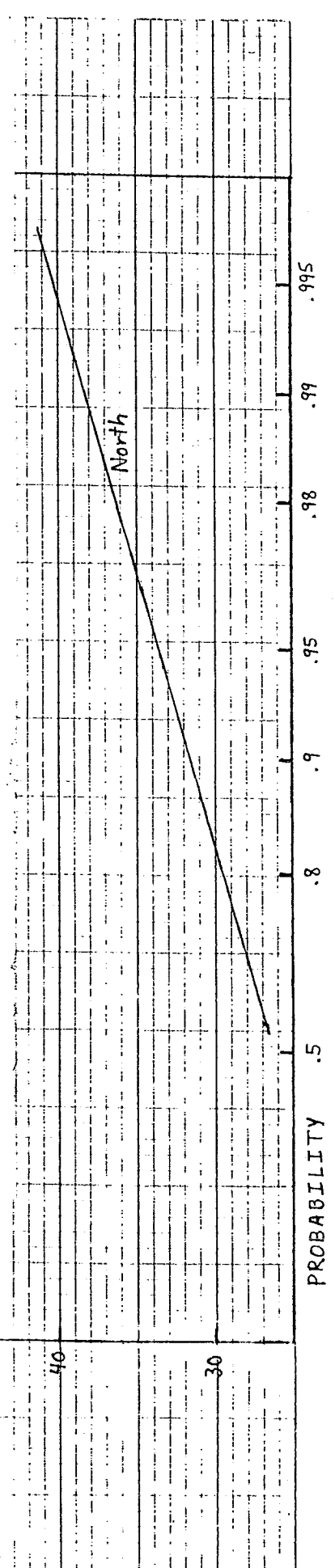Fig. 2. Return periods for one-minute extreme north and south winds at a height of 30 ft.

Fig. 3. Return periods for one-minute extreme north and south winds at a height of 30 ft.
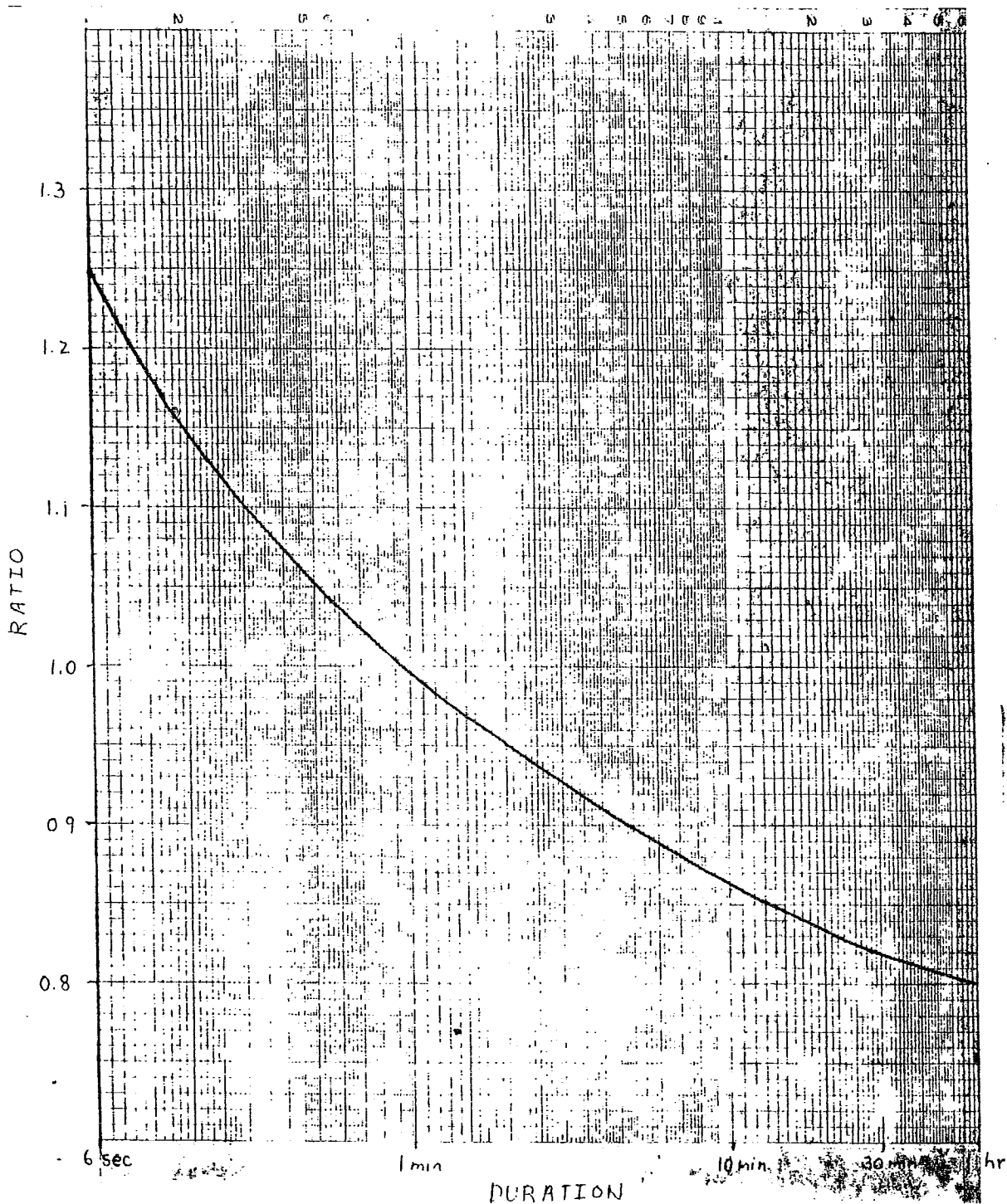
Figure 4. Ratio of average wind speed of given duration to the one-minute average speed.